The Astrophysical Journal, 739:45 (24pp), 2011 September 20 doi:10.1088/0004-637X/739/1/45

CONSTRAINTS ON THE ASSEMBLY AND DYNAMICS OF GALAXIES. II. PROPERTIES OF KILOPARSEC-SCALE CLUMPS IN REST-FRAME OPTICAL EMISSION OF $z \sim 2$ STAR-FORMING GALAXIES*

N. M. Förster Schreiber[1], A. E. Shapley[2,13], R. Genzel[1,3], N. Bouché[4,5,6,14], G. Cresci[7], R. Davies[1], D. K. Erb[8], S. Genel[1,9], D. Lutz[1], S. Newman[10], K. L. Shapiro[10,11], C. C. Steidel[12], A. Sternberg[9], and L. J. Tacconi[1]
[1] Max-Planck-Institut für extraterrestrische Physik, Giessenbachstrasse, D-85748 Garching, Germany
[2] Department of Physics and Astronomy, University of California, Los Angeles, CA 90095-1547, USA
[3] Department of Physics, Le Conte Hall, University of California, Berkeley, CA 94720, USA
[4] Department of Physics, University of California Santa Barbara, Santa Barbara, California, CA 93106-9530, USA
[5] CNRS, Institut de Recherche en Astrophysique et Planétologie de Toulouse, 14 Avenue E. Belin, F-31400 Toulouse, France
[6] Université de Toulouse, UPS-OMP, IRAP, F-31400 Toulouse, France
[7] INAF-Osservatorio Astrofisico di Arcetri, Largo E. Fermi 5, I-50125 Firenze, Italy
[8] Department of Physics, University of Wisconsin Milwaukee, Milwaukee, Wisconsin, WI 53211, USA
[9] Sackler School of Physics & Astronomy, Tel Aviv University, Tel Aviv 69978, Israel
[10] Department of Astronomy, Campbell Hall, University of California, Berkeley, CA 94720, USA
[11] Aerospace Research Laboratories, Northrop Grumman Aerospace Systems, Redondo Beach, CA 90278, USA
[12] California Institute of Technology, MS 105-24, Pasadena, CA 91125, USA
Received 2011 April 1; accepted 2011 July 4; published 2011 September 6

ABSTRACT

We study the properties of luminous stellar "clumps" identified in deep, high-resolution *Hubble Space Telescope* NIC2/F160W imaging at 1.6 μm of six $z \sim 2$ star-forming galaxies with existing near-infrared integral field spectroscopy from SINFONI at the Very Large Telescope. Individual clumps contribute ∼0.5%–15% of the galaxy-integrated rest-frame ≈5000 Å emission, with median of ≈2%; the total contribution of clump light ranges from 10% to 25%. The median intrinsic clump size and stellar mass are ∼1 kpc and $\sim 10^9\ M_\odot$, in the ranges for clumps identified in rest-UV or line emission in other studies. The clump sizes and masses in the subset of disks are broadly consistent with expectations for clump formation through gravitational instabilities in gas-rich, turbulent disks given the host galaxies' global properties. By combining the NIC2 data with Advanced Camera for Surveys (ACS)/F814W imaging available for one source, and adaptive-optics-assisted SINFONI Hα data for another, we infer modest color, M/L, and stellar age variations within each galaxy. In these two objects, sets of clumps identified at different wavelengths do not fully overlap; NIC2-identified clumps tend to be redder/older than ACS- or Hα-identified clumps without rest-frame optical counterparts. There is evidence for a systematic trend of older ages at smaller galactocentric radii among the clumps, consistent with scenarios where inward migration of clumps transports material toward the central regions. From constraints on a bulge-like component at radii $\lesssim$1–3 kpc, none of the five disks in our sample appears to contain a compact massive stellar core, and we do not discern a trend of bulge *stellar* mass fraction with stellar age of the galaxy. Further observations are necessary to probe the buildup of stellar bulges and the role of clumps in this process.

Key words: galaxies: evolution – galaxies: high-redshift – galaxies: structure – infrared: galaxies

Online-only material: color figures

1. INTRODUCTION

Luminous, kiloparsec (kpc)-sized "clumps" appear to be a ubiquitous feature of high-redshift star-forming galaxies. Such clumps have long been discussed in the context of high-resolution imaging of distant objects (e.g., Cowie et al. 1995; van den Bergh et al. 1996; Colley et al. 1996; Giavalisco et al. 1996; Elmegreen et al. 2004a, 2004b; Elmegreen & Elmegreen 2005; Conselice et al. 2004; Lotz et al. 2004; Papovich et al. 2005; Law et al. 2007). They have been mostly identified in optical imaging from the *Hubble Space Telescope* (*HST*), probing rest-frame UV wavelengths at $z \gtrsim 1$. High-resolution *HST* near-infrared (near-IR) observations with the NICMOS camera, and most recently with the WFC3 instrument, show that clumpy structures can also be present in the rest-frame optical (e.g., Toft et al. 2007; Dasyra et al. 2008; Kriek et al. 2009; Elmegreen et al. 2009a; Bussmann et al. 2009; Swinbank et al. 2010a; Overzier et al. 2010; Cameron et al. 2010). Similar clumps have been identified in rest-frame optical line emission from near-IR integral field spectroscopy of several $z \sim 2$ disks (Genzel et al. 2006, 2008, 2011). Observations of strongly lensed $z \sim$ 1–3 sources in broadband rest-UV/optical light, rest-optical line emission, and submillimeter dust continuum and CO line emission with source-plane resolution down to ∼100 pc have confirmed characteristic sizes for stellar clumps and star-forming complexes of ∼300 pc to 1 kpc (e.g., Stark et al. 2008; Jones et al. 2010; Swinbank et al. 2010b).

Various lines of evidence suggest that these clumps are not only associated with distinct components in merging or interacting systems. They are found in all types of galaxies at $z \gtrsim 1$, including disks identified as such on the basis of their

* Based on observations made with the NASA/ESA *Hubble Space Telescope*, obtained at the Space Telescope Science Institute, which is operated by the Association of Universities for Research in Astronomy, Inc., under NASA contract NAS 5-26555. These observations are associated with program no. 10924. Also based on observations obtained at the Very Large Telescope of the European Southern Observatory, Paranal, Chile (ESO Programme IDs 073.B-9018, 074.A-9011, 075.A-0466, 076.A-0527, 077.A-0576, 078.A-0600, 079.A-0341, 080.A-0330, and 080.A-0339).
[13] Packard Fellow.
[14] Marie Curie Fellow.

structural properties (Elmegreen & Elmegreen 2005; Elmegreen et al. 2005, 2007, 2009a) as well as their kinematics (Genzel et al. 2006, 2008, 2011; Bournaud et al. 2008; Jones et al. 2010). High-redshift disks are found to have high gas-to-total-baryonic mass fractions of ∼20%–80% and high local intrinsic gas velocity dispersions of ∼20–90 km s^{-1} (e.g., Erb et al. 2006; Förster Schreiber et al. 2006, 2009; Genzel et al. 2008; Cresci et al. 2009; Épinat et al. 2009; Law et al. 2009; Wright et al. 2009; Daddi et al. 2010; Tacconi et al. 2010). Numerical simulations of gas-rich turbulent disks indicate that massive kpc-sized clumps can form in situ through gravitational instabilities (e.g., Noguchi 1999; Immeli et al. 2004a, 2004b; Bournaud et al. 2007; Elmegreen et al. 2008; Dekel et al. 2009; Agertz et al. 2009; Ceverino et al. 2010; Aumer et al. 2010; Genel et al. 2010). The Toomre length and mass derived from the global properties of clumpy disks at high redshift correspond roughly to the clump sizes and masses inferred from observations (e.g., Genzel et al. 2008, 2011; Bournaud et al. 2008; Elmegreen et al. 2009a; Jones et al. 2010). In these numerical simulations, and according to theoretical arguments, the clumps can migrate toward the gravitational center as a result of their mutual interactions and of dynamical friction against the host disk, and coalesce into a young bulge on timescales of ∼1 Gyr. They may also lose part of their mass, contributing to the redistribution of mass and angular momentum and to the growth of the disk.

This "clump-driven" scenario has gained popularity and empirical support in recent years as an important mechanism for the early formation phases of the spheroidal and disk components of present-day massive galaxies. One of the major uncertainties in this scenario is the survival of clumps against the disruptive effects of tidal torques and of stellar feedback, both radiative and mechanical (Murray et al. 2010; Krumholz & Dekel 2010; Genel et al. 2010; Genzel et al. 2011). Characterizing in detail the properties of individual clumps in distant galaxies, such as their masses, ages, star formation histories (SFHs), and spatial distribution across the host galaxy, is crucial to address this issue but remains obviously very challenging because of the sensitivity and high spatial resolution required.

In this paper, we study clumps identified in the *rest-frame optical* emission in six massive star-forming $z = 2.1$–2.5 galaxies, for which we obtained deep high-resolution *HST* imaging at 1.6 μm with the NICMOS/NIC2 camera and F160W filter. The targets are among the rest-UV-selected sources observed with SINFONI as part of the SINS survey (Förster Schreiber et al. 2006, 2009). In a companion paper (Förster Schreiber et al. 2011, hereafter Paper I), we derived the structural and morphological parameters of the targets from the NIC2 imaging, analyzed the results together with the Hα line maps and kinematics from SINFONI, and compared the morphological properties with those of other samples of massive $z \sim 2$ galaxies imaged with NIC2/F160W but selected very differently and probing a wide range in star formation activity. All but one of our SINS NIC2 targets exhibit compelling kinematic signatures of disk rotation. The global rest-frame optical surface brightness distributions indicate disk-dominated morphologies as well, with Sérsic indices in the range $n \approx 0.15$–2. In contrast, the kinematics of the sixth source unambiguously reveal a major merger, the main components of which are well resolved in the NIC2 imaging. Here, we analyze the prominent kpc-scale structures seen in all our targets. The combination of SINFONI and NIC2 data sets enables us to determine whether observed clumps represent structures consistent with in situ formation through disk instabilities or, instead, whether they are associated with merging components. We focus on the stellar properties of the clumps in order to constrain their evolution and role in early bulge formation. Two objects are studied in more detail, taking advantage of additional high-resolution *HST* optical imaging available for one, and SINFONI observations together with adaptive optics (AO) for the other.

The paper is organized as follows. We present the selection and global properties of the sample, and summarize the NICMOS/NIC2 observations and data reduction in Section 2. We describe the identification procedure and derive the main properties of clumps in the NIC2 images in Section 3. In Section 4, we focus on detailed case studies of the target with existing high-resolution *HST* optical imaging (SSA22a−MD 41) and the one with AO-assisted Hα SINFONI observations (Q2346−BX 482), and further constrain spatial variations in colors, stellar-mass-to-light ratios, and stellar ages. The implications of our results for the formation and evolution of clumps are discussed in Section 5. The paper is summarized in Section 6. Throughout, we assume a Λ-dominated cosmology with $H_0 = 70\,h_{70}$ km s^{-1} Mpc^{-1}, $\Omega_m = 0.3$, and $\Omega_\Lambda = 0.7$. For this cosmology, 1″ corresponds to ≈8.2 kpc at $z = 2.2$. Magnitudes are given in the AB photometric system unless otherwise specified.

2. SAMPLE, OBSERVATIONS, AND DATA REDUCTION

2.1. NIC2 Target Selection and Ancillary Data

Table 1 lists the six galaxies studied in this paper. The targets were drawn from the initial sample of 17 rest-UV-selected objects at $z \sim 2$ from the SINS survey (Förster Schreiber et al. 2006, 2009) carried out with the near-IR integral field spectrometer SINFONI (Eisenhauer et al. 2003; Bonnet et al. 2004) at the ESO Very Large Telescope (VLT). The galaxies were originally part of the large optical spectroscopic survey of $z \sim 1.5$–2.5 candidates selected by their $U_n G\mathcal{R}$ colors described by Steidel et al. (2004). Additional multi-wavelength data include ground-based near-IR J- and K_s-band imaging, and space-based *Spitzer* mid-IR photometry at 3–8 μm with Infrared Array Camera (IRAC) and at 24 μm with Multiband Imaging Photometer for *Spitzer* (MIPS) for the majority of our targets (Erb et al. 2006; Reddy et al. 2010). For one galaxy, MD 41, high-resolution optical imaging is available from observations with the *HST* Advanced Camera for Surveys (ACS) through the F814W filter (hereafter i_{814} bandpass).

The choice of our NIC2 targets was primarily driven by their kinematic nature along with their high signal-to-noise (S/N), high-quality SINFONI data mapping the spatial distribution and relative gas motions from the Hα line emission out to radii $\gtrsim$10 kpc. Five of the targets (BX 663, MD 41, BX 389, BX 610, and BX 482) were explicitly selected because of their disk-like kinematics, and the sixth one (BX 528) because it shows, in contrast, kinematic signatures consistent with a counter-rotating binary merger. The galaxies are among the brighter and larger half of the full SINS sample in terms of Hα flux and size (see Paper I). The quantitative kinematic classification was performed through application of kinemetry by Shapiro et al. (2008), and detailed dynamical modeling of the disks is presented by Genzel et al. (2008) and Cresci et al. (2009).

The SINFONI data sets of our NIC2 targets, among the deepest of the SINS survey, are fully described by Förster Schreiber et al. (2006, 2009). Briefly, all galaxies were observed in the K band (targeting the Hα and [N II] $\lambda\lambda$6548, 6584 emission lines) using the largest pixel scale of 125 mas pixel^{-1},

Table 1
Galaxies Observed

Property	Q1623−BX 528	Q1623−BX 663[a]	SSA22a−MD 41	Q2343−BX 389	Q2343−BX 610[a]	Q2346−BX 482
$z_{H\alpha}$[b]	2.2683	2.4332	2.1704	2.1733	2.2103	2.2571
H_{160} (mag)[c]	22.33 ± 0.06	22.79 ± 0.10	22.64 ± 0.05	23.11 ± 0.10	22.09 ± 0.06	22.34 ± 0.07
Age (Myr)[d]	2750^{+96}_{-2110}	2500^{+147}_{-800}	50^{+31}_{-0}	2750^{+224}_{-1945}	2750^{+173}_{-650}	321^{+485}_{-141}
A_V (mag)[d]	0.6 ± 0.2	0.8 ± 0.2	1.2 ± 0.2	1.0 ± 0.2	0.8 ± 0.2	0.8 ± 0.2
$M_\star$ (10^{10} $M_\odot$)[d]	$6.95^{+0.17}_{-3.61}$	$6.40^{+0.22}_{-2.28}$	$0.77^{+0.10}_{-0.03}$	$4.12^{+0.77}_{-2.16}$	$10.0^{+2.7}_{-0.6}$	$1.84^{+0.79}_{-0.46}$
$M_\star/L_g^{\rm rest}$ ($M_\odot$ $L_{g,\odot}^{-1}$)[d]	0.51	0.58	0.08	0.78	0.63	0.15
SFR ($M_\odot$ yr^{-1})[d]	42^{+29}_{-16}	42^{+13}_{-12}	185^{+3}_{-70}	25^{+17}_{-2}	60^{+26}_{-1}	80^{+42}_{-32}
sSFR (Gyr^{-1})[d]	$0.6^{+1.7}_{-0.1}$	$0.7^{+0.3}_{-0.2}$	24^{+1}_{-9}	$0.6^{+1.2}_{-0.1}$	0.6 ± 0.2	$4.3^{+3.0}_{-2.5}$
Kinematic type[e]	Major merger	Disk	Disk	Disk	Disk	Disk
R_e (kpc)[f]	$4.86^{+0.13}_{-0.10}$	$4.54^{+7.71}_{-0.79}$	$5.69^{+0.20}_{-0.13}$	$5.93^{+0.17}_{-0.12}$	4.44 ± 0.08	$6.22^{+0.13}_{-0.12}$
n[f]	0.16 ± 0.01	$2.00^{+2.11}_{-0.59}$	$0.54^{+0.07}_{-0.06}$	$0.36^{+0.07}_{-0.05}$	0.57 ± 0.04	0.14 ± 0.01
b/a[f]	0.31 ± 0.01	$0.73^{+0.04}_{-0.02}$	0.31 ± 0.01	0.30 ± 0.01	0.56 ± 0.01	0.48 ± 0.01

Notes.

[a] Spectral signatures of a Type 2 AGN are detected in the optical and near-IR spectrum of BX 663 and the large-scale Hα kinematics suggest that the host galaxy is a low-inclination rotating disk (Erb et al. 2006; Förster Schreiber et al. 2006, 2009). The *Spitzer*/MIPS 24 μm flux in BX 663 is consistent with obscured AGN activity. A 24 μm excess is also detected for BX 610 but since there is no other signature of AGN activity in this galaxy, it could be due to enhanced mid-IR PAH emission around rest-frame 8 μm instead (see Section 2.2).

[b] Systemic vacuum redshift derived from the integrated Hα line emission (Förster Schreiber et al. 2009).

[c] The H_{160}-band magnitudes (AB system) measured from the NIC2 data in a circular aperture with diameter of 3″.

[d] Stellar age, visual extinction (A_V), stellar mass ($M_\star$), stellar mass to rest-frame SDSS g-band luminosity ratio ($M_\star/L_g^{\rm rest}$, uncorrected for extinction), and absolute and specific star formation rate (SFR and sSFR) of the best-fit evolutionary synthesis model to the observed optical to near-IR photometry of the galaxies. The SEDs were fitted using Bruzual & Charlot (2003) models with solar metallicity, a Chabrier (2003) IMF, the Calzetti et al. (2000) reddening law, and a constant SFR. The formal (random) fitting uncertainties listed are derived from the 68% confidence intervals based on 200 Monte Carlo simulations; systematic uncertainties (from SED modeling assumptions) are estimated to be typically a factor of 1.5 for the stellar masses, ±0.3 mag for the extinctions, and factors of ∼2–3 for the ages as well as for the absolute and specific star formation rates.

[e] Classification according to the Hα kinematics from SINFONI (Shapiro et al. 2008; Förster Schreiber et al. 2006, 2009).

[f] Effective radius, light concentration index, and ratio of minor to major axis (R_e, n, b/a) obtained from single-component Sérsic model fits to the two-dimensional H_{160}-band surface brightness distributions of the galaxies; the best-fit parameters correspond to the median of the distribution of results from 500 GALFIT runs as described in Paper I, and the uncertainties represent the 68% confidence intervals around the best-fit value. For BX 528, the two main merging components "SE" and "NW" are resolved in the NIC2 data; the results of simultaneous two-component Sérsic model fits are $R_e = 3.18^{+0.18}_{-0.25}$, $n = 1.20^{+0.15}_{-0.19}$, and $b/a = 0.35^{-0.08}_{-0.03}$ for BX 528−SE, and $R_e = 3.57^{+1.98}_{-0.57}$, $n = 2.91^{+1.70}_{-1.34}$, and $b/a = 0.51^{+0.06}_{-0.05}$ for BX 528−NW. For BX 389, the NIC2 data resolve the small companion south of the main part of the galaxy; the results of simultaneous two-component Sérsic model fits are $R_e = 5.89^{+0.08}_{-0.09}$, $n = 0.32^{+0.04}_{-0.04}$, and $b/a = 0.27 \pm 0.01$ for the main body of BX 389, and $R_e = 2.71^{+2.18}_{-0.69}$, $n = 3.03^{+2.64}_{-1.75}$, and $b/a = 0.20^{+0.35}_{-0.16}$ for BX 389−South.

five of them in seeing-limited mode with FWHM spatial resolution of ≈0.″5 (corresponding to ≈4.1 kpc) and one of them, BX 663, with the aid of AO resulting in a resolution of 0.″39 (or 3.2 kpc). Seeing-limited H-band data at the 125 mas pixel^{-1} scale were taken for all but BX 528 to map the Hβ and [O III] λλ4959, 5007 emission lines, also under very good near-IR seeing of ≈0.″55. For BX 482, AO-assisted K-band observations were obtained using the intermediate pixel scale of 50 mas pixel^{-1}, with a total on-source integration time of 6.8 hr and resolution of 0.″17 (1.4 kpc), very similar to that of the NIC2 1.6 μm imaging.

2.2. Global Properties of the NIC2 Targets

Our NIC2 sample is relatively bright in the near-IR. The five objects with existing K-band imaging have a median $K_{s,AB} = 21.8$ mag and span a range of ≈1.2 mag in observed K band as well as in rest-frame absolute V band ($K_{s,AB} =$ 21.1–22.3 mag, and $M_{V,AB}$ between −23.1 and −21.9 mag; see Paper I). *Spitzer*/MIPS 24 μm measurements that have been obtained for four of the targets (BX 389, BX 610, BX 528, and BX 663) indicate that they are among the 3% most luminous at rest-frame 8 μm wavelengths of UV-selected $z \sim 2$ galaxies (Reddy et al. 2010).

In terms of global stellar properties, our NIC2 targets probe the actively star-forming part of the massive $z \sim 2$ galaxy population (Erb et al. 2006; Förster Schreiber et al. 2009). Modeling of their optical to near-IR spectral energy distributions (SEDs), including the new photometry obtained with NIC2, is described in Paper I. The results using the Bruzual & Charlot (2003) evolutionary synthesis code, assuming constant star formation (CSF), solar metallicity, and adopting the Chabrier (2003) initial mass function (IMF) and the Calzetti et al. (2000) reddening law, are given in Table 1. The stellar masses span over an order of magnitude, from 7.7×10^9 to 1.0×10^{11} $M_\odot$ with median $\approx 5 \times 10^{10}$ $M_\odot$. The median absolute and specific star formation rates (SFRs) are ≈50 $M_\odot$ yr^{-1} and 0.7 Gyr^{-1} (with ranges of 25–185 $M_\odot$ yr^{-1} and 0.6–24 Gyr^{-1}). The objects are moderately obscured, with A_V between 0.6 and 1.2 mag, or equivalently $E(B-V) = 0.15$–0.30 mag. The stellar ages range from 50 Myr to 2.75 Gyr; BX 528, BX 663, BX 389, and BX 610 have ages comparable to the age of the universe at their redshift, indicating that they host mature stellar populations. The best-fit models to the SEDs of these four objects imply rest-frame $(U-B)_{AB} \approx 0.75$–0.9 mag colors, close to or just about at the separation adopted by, e.g., Kriek et al. (2009), between "red" and "blue" objects. In contrast, the two youngest objects, MD 41 and BX 482, are significantly bluer with rest-frame $(U-B)_{AB} \approx 0.5$ mag.

Two of our targets (BX 663 and BX 610) are identified as candidate active galactic nucleus (AGN) on the basis of their observed mid-IR SEDs from *Spitzer* IRAC and MIPS photometry (Reddy et al. 2010). BX 663 also exhibits spectral signatures of Type 2 AGN in its integrated rest-frame UV and optical spectra (Shapley et al. 2004; Erb et al. 2006). In our spatially resolved SINFONI data, the central compact emission peak of BX 663 is characterized by a higher [N II]/Hα and a broad Hα velocity component associated with the AGN, underneath the narrower component dominated by star formation. In contrast, BX 610 exhibits no sign of an AGN in the rest-frame UV and optical, so that its putative AGN is likely to be very obscured and will not affect any aspect of our analysis. Alternatively, its mid-IR emission properties could be due to enhanced polycyclic aromatic hydrocarbon (PAH) emission around rest-frame 8 μm with respect to its far-IR luminosity and in comparison to local star-forming galaxies of the same total luminosity, as indicated by recent measurements of the full mid- to far-IR SEDs of high-z star-forming galaxies (e.g., Nordon et al. 2010, 2011; Elbaz et al. 2010; Muzzin et al. 2010; Wuyts et al. 2011). In the context of this paper, we will only consider BX 663 explicitly as an AGN source.

As described in Paper I, our NIC2 targets do not stand out compared to the full SINS sample in terms of global stellar and dust properties but they do more so in terms of their observed Hα properties. This is a consequence of our emphasis on selecting objects for the NIC2 follow-up with highest S/N and spatially best-resolved Hα emission from the initial seeing-limited SINFONI data sets from the SINS survey. The median stellar mass and SFR of our NIC2 targets are comparable to those of the SINS Hα sample ($\approx 3 \times 10^{10}\,M_\odot$ and $\approx 70\,M_\odot\,\mathrm{yr}^{-1}$). However, they are among the brighter half in terms of integrated Hα fluxes (uncorrected for extinction) with median $F(\mathrm{H}\alpha) = 1.9 \times 10^{-16}\,\mathrm{erg\,s^{-1}\,cm^{-2}}$ (and range from 1.1 to $3.1 \times 10^{-16}\,\mathrm{erg\,s^{-1}\,cm^{-2}}$), compared with the SINS Hα sample median of $F(\mathrm{H}\alpha) = 1.1 \times 10^{-16}\,\mathrm{erg\,s^{-1}\,cm^{-2}}$. Our NIC2 targets also lie at the high end of the Hα velocity–size distribution (Bouché et al. 2007; Förster Schreiber et al. 2009). Their intrinsic half-light radii $r_{1/2}(\mathrm{H}\alpha) \approx 4$–5 kpc are above the SINS sample median of 3.1 kpc, and the circular velocities v_d for the five disks are equal to or larger than the median for SINS galaxies of $\approx 180\,\mathrm{km\,s^{-1}}$, and up to $\sim 300\,\mathrm{km\,s^{-1}}$.[15] The ratio of circular velocity to intrinsic local velocity dispersion of these disks are in the range $v_\mathrm{c}/\sigma_0 \approx 2$–6 (Genzel et al. 2008; Cresci et al. 2009; Förster Schreiber et al. 2009), which is significantly lower than for local spiral galaxies (with typical $v_\mathrm{c}/\sigma_0 \sim 10$–20; e.g., Dib et al. 2006; Épinat et al. 2010). These low ratios suggest comparatively larger gas turbulence and geometric thickness and appear to be a characteristic feature of early disk galaxies at $z \sim 1$–3 (e.g., Förster Schreiber et al. 2006; Wright et al. 2007; Genzel et al. 2008; Stark et al. 2008; Cresci et al. 2009; Épinat et al. 2009; Jones et al. 2010).

2.3. NICMOS/NIC2 Observations and Data Reduction

The spatial extent and brightness of our targets make them particularly well suited for a detailed study of morphologies and a reliable assessment of structural parameters from high-resolution rest-frame optical continuum imaging (Paper I). Sensitivity and adequate sampling of the instrumental point-spread function (PSF) are essential for these purposes, as well as for identifying and characterizing small-scale structure, the subject of this paper. These goals dictated our observational strategy and the procedures applied for data reduction, PSF characterization, and analysis of the noise properties, which are detailed in Paper I and summarized in this subsection.

The NICMOS observations were carried out between 2007 April and 2007 September with the NIC2 camera on board the *HST* and using the F160W filter with mean wavelength of 1.61 μm (hereafter H_{160} bandpass). NIC2 has a pixel scale of 0.″075, critically sampling the *HST* PSF at 1.6 μm. The H_{160} bandpass probes rest-frame optical wavelengths around 5000 Å at the median $z = 2.23$ of our targets, and corresponds closely to the Sloan Digital Sky Survey (SDSS) g band (which is about 300 Å bluer in the rest frame). At these wavelengths, redward of the 4000 Å/Balmer break, the galaxies' light traces the bulk of stellar mass more reliably than the rest-frame UV, which is significantly more affected by recent star formation and by dust extinction. Each target was observed for four orbits, amounting to a total on-source integration time of 10,240 s with good sampling of the PSF.

The data were reduced using standard routines of the NICMOS pipeline within the IRAF environment, complemented with custom procedures to optimize the removal of bad pixels and cosmic-ray hits, and of large-scale residuals across the images. The images were drizzled onto a final pixel scale of $0.''05\,\mathrm{pixel}^{-1}$. The PSF was determined empirically from the two-dimensional profiles of the four brightest, unsaturated, and isolated stars present in our NIC2 pointings, and has an FWHM of 0.″145 based on a Gaussian profile fit. The effective noise properties were characterized from the final reduced images, taking into account deviations from pure Gaussian noise due to instrumental features as well as correlated noise and systematics resulting from the data reduction procedure. The 3σ limiting surface brightness of the final images is $\mu(H_{160,\mathrm{AB}}) = 23.4\,\mathrm{mag\,arcsec^{-2}}$, and the 3σ limiting magnitude in a "point-source aperture" with diameter $d = 1.5 \times \mathrm{PSF\,FWHM} = 0.''22$ (maximizing the S/N of photometric measurements in unweighted circular apertures of point-like sources) is ≈ 28.1 mag. The total H_{160}-band magnitudes measured in a circular aperture with diameter of 3″ centered on each target are reported in Table 1.

Figure 1 presents the final reduced images of the galaxies with sampling of $0.''05\,\mathrm{pixel}^{-1}$. The angular resolution of FWHM = 0.″145 corresponds to a spatial resolution of ≈ 1.2 kpc at the redshifts of our targets. The geometric center calculated as the unweighted mean of the x- and y-coordinates of pixels with S/N $\geqslant 3$ is indicated by a cross in Figure 1. For the five disks, it corresponds closely to the dynamical center based on modeling of the Hα kinematics (Genzel et al. 2008; Cresci et al. 2009). In H_{160}-band (rest frame $\approx$5000 Å) emission, the galaxies exhibit a diffuse and lower-surface-brightness component extending out to radii of 0.″8–1.″2 or 6.5–10 kpc. Rich substructure, including several bright compact emission regions, is seen in all sources and contributes to their irregular appearance. For BX 528, two major emission sources to the southeast and northwest are well resolved in the NIC2 images (denoted BX 528−SE and NW, with projected separation of 8 kpc), with relative H_{160}-band fluxes that suggest a nearly equal-mass major merger (mass ratio of $\sim$1.5:1), in agreement with the kinemetry analysis of the Hα kinematics (Shapiro et al. 2008). For the large disk, BX 389, the small and faint companion 5 kpc in projection to the south of the galaxy and at nearly the same redshift as its main part signals a minor merger (mass ratio of $\sim$10:1),

[15] The merger BX 528 has a lower equivalent v_d of $145\,\mathrm{km\,s^{-1}}$; see Förster Schreiber et al. (2009) for the derivation.

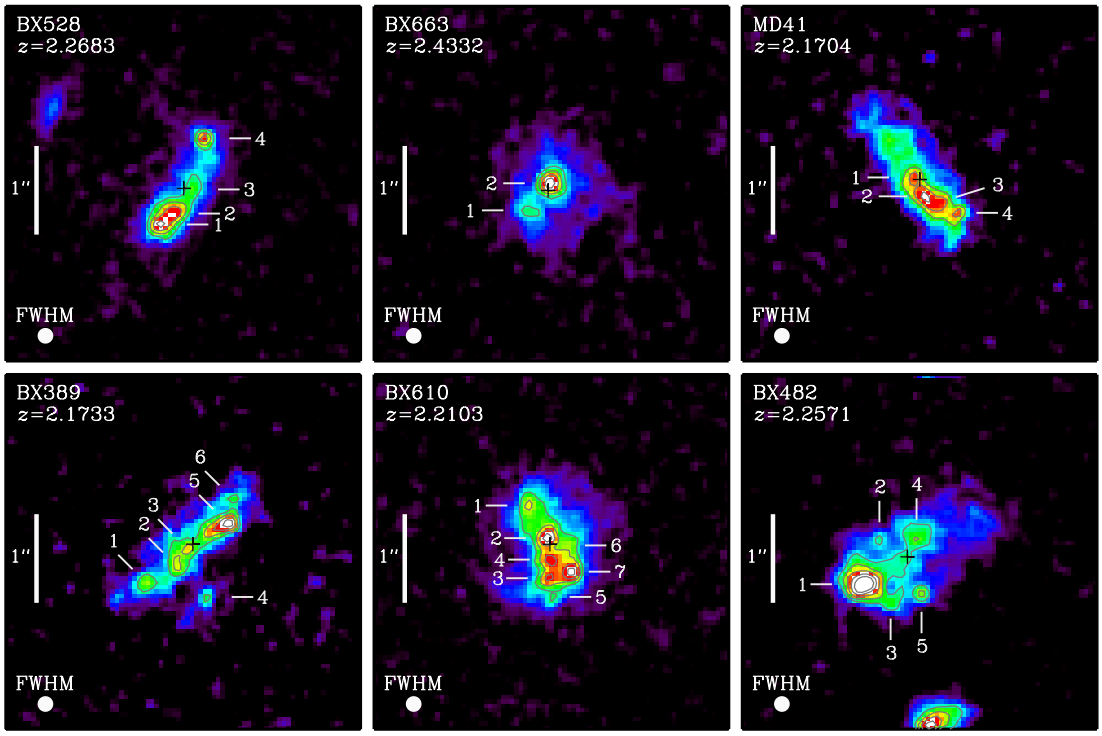

Figure 1. *HST* NICMOS/NIC2 H_{160}-band maps of the galaxies, probing the broadband emission around rest frame 5000 Å. The target name and Hα redshift are labeled in the top corner of each panel. The color coding scales linearly with flux density from black to white for the minimum to maximum levels displayed (varying for each galaxy). Contours are overplotted starting at flux densities ≈50% of the maximum in each image. The FWHM of the effective PSF is indicated by the filled circle at the bottom left of each corner; the angular resolution is 0.″145 or ≈1.2 kpc at the median $z = 2.2$ of the sources. The angular scale of the images is shown with the 1″long vertical bar next to each galaxy. In all maps, north is up and east is to the left. The compact clumps identified in each galaxy are indicated, with their ID number labeled.

(A color version of this figure is available in the online journal.)

consistent with the lack of substantial disturbances in the Hα kinematics.

3. PROPERTIES OF CLUMPS IDENTIFIED IN THE REST-FRAME OPTICAL

In Paper I, we quantified the overall structural properties of our NIC2 targets using both parametric and non-parametric methods. We compared the rest-frame optical and Hα morphologies (as well as the rest-frame UV morphology for MD 41), and also made a differential comparison with other samples of massive galaxies at the same redshift but selected using different photometric criteria. The effective radius R_e, Sérsic index n, and ratio of minor to major axis b/a derived from single-component Sérsic model fits to the H_{160}-band maps of our targets are given in Table 1. Now, we turn to the prominent and widely distributed clumpy features that constitute one of the most striking aspects of the rest-frame optical morphologies of our SINS NIC2 galaxies. In what follows, we use the term "clump" to refer generically to any small-scale feature identified with the method described below. This method also recovers the merger components of BX 528 as clumps, as well as the southern companion of BX 389 and the central peak of the AGN-hosting BX 663.

3.1. Clump Identification and Measurements

To identify clumps as objectively as possible, and in the same way for all our galaxies, we used the IRAF task *daofind* (Stetson 1987). This task is optimized for identification of compact or point-like sources in crowded fields with variable underlying background emission, and is thus appropriate for our purposes. This task detects objects by searching for local density maxima with specified FWHM and peak amplitudes above the local background. We used a detection threshold of $\geqslant 3\sigma$ (with σ being the pixel-to-pixel rms noise) and, given the observed extent of the bright clumps, we set the characteristic scales to (1–1.5)× the PSF FWHM. Because the clumps are not strictly point sources and have a range of sizes, brightnesses, and brightness contrasts against the host galaxies' "background," the number of clumps depends slightly on the exact values for the threshold and size scale. Based on experimentation, we found that the choices above were the most satisfactory according to a visual assessment, and we used the same values for all galaxies. A total of 28 clumps are identified, with between two and seven per source, and are indicated on the NIC2 maps in Figure 1. They are listed in Table 2 along with their projected distance $d_{\rm proj}$ from the geometric center of the galaxies (coinciding with the dynamical center) and other properties derived below. We also calculated the deprojected galactocentric distance d assuming the clumps are confined to a disk of inclination with respect to the sky plane given by the best-fit morphological axis ratio of each galaxy (Table 1). As seen in Figure 1, the two main components of the interacting system BX 528 correspond to the neighboring clumps 1 and 2 (BX 528−SE) and to clump 4 (BX 528−NW). The central peak of BX 663 is identified as clump 2, and the southern companion of BX 389 as clump 4.

Measurements of the clump sizes and brightnesses in our NIC2 images are complicated by the bright and variable background from the host galaxy, and by the close proximity of neighboring clumps often with relatively few resolution elements sampling both clumps and interclump regions. Moreover, large-scale asymmetries in the global light distribution of some of the galaxies affect the accuracy of the clump properties if

Table 2
Properties of Clumps Identified in the NIC2 Images

Clump[a]	$d_{\rm proj}$[b] (kpc)	d[b] (kpc)	$r_{\rm phot}$[c] (arcsec)	Ap. corr.[c]	FWHM[d]	FWHM^0[d] (kpc)	$\mathcal{F}^{\rm cl}_{\rm PS}$[e]	$\mathcal{F}^{\rm cl}_{\rm raw}$[e]	$\mathcal{F}^{\rm cl}$[e]	$H^{\rm cl}_{160}$[f] (mag)	$L^{\rm rest,cl}_{g}$[g] ($L_{g,\odot}$)	$M^{\rm cl}_{\star}$[h] ($M_{\odot}$)
Q1623−BX 528												
1	3.92	4.0 ± 0.3	0.125	1.79	1.23	0.31	0.016	0.093	0.052	25.53	6.5×10^9	3.6×10^9
2	2.52	2.6 ± 0.3	0.125	1.79	1.52	0.94	0.011	0.092	0.040	25.82	5.0×10^9	2.8×10^9
3	0.86	2.6 ± 0.5	0.125	1.79	1.27	0.43	0.008	0.054	0.023	26.42	2.9×10^9	1.6×10^9
4	5.02	5.2 ± 0.6	0.200	1.44	1.35	0.64	0.022	0.108	0.077	25.11	9.7×10^9	5.4×10^9
All	...	...	...	...	...	...	0.057	0.347	0.193	...	...	...
Q1623−BX 663												
1	2.56	2.7 ± 0.7	0.100	2.09	<1.18	...	0.008	0.035	0.012	27.62	1.1×10^9	7.5×10^8
2	0.68	0.68 ± 0.08	0.225	1.33	1.81	1.37	0.022	0.209	0.132	24.99	1.2×10^{10}	8.4×10^9
All	...	...	...	...	...	...	0.030	0.244	0.143	...	...	...
SSA22a−MD 41												
1	0.56	1.1 ± 0.2	0.100	2.09	<1.20	...	0.008	0.038	0.017	27.08	1.5×10^9	1.3×10^8
2	1.65	2.3 ± 0.2	0.100	2.09	<1.20	...	0.009	0.044	0.021	26.82	1.9×10^9	1.6×10^8
3	2.96	3.2 ± 0.1	0.100	2.09	<1.20	...	0.006	0.039	0.012	27.45	1.0×10^9	9.2×10^7
4	4.77	5.8 ± 0.4	0.100	2.09	<1.20	...	0.011	0.036	0.026	26.58	2.3×10^9	2.0×10^8
All	...	...	...	...	...	...	0.035	0.156	0.076	...	...	...
Q2343−BX 389												
1	5.65	5.7 ± 0.1	0.175	1.53	1.74	1.26	0.009	0.077	0.043	26.53	2.4×10^9	1.8×10^9
2	2.57	3.3 ± 0.4	0.150	1.63	1.72	1.23	0.008	0.070	0.030	26.92	1.7×10^9	1.2×10^9
3	0.67	0.77 ± 0.06	0.125	1.79	<1.20	...	0.009	0.054	0.021	27.29	1.2×10^9	8.8×10^8
4	5.10	...	0.175	1.53	1.38	0.69	0.012	0.046	0.032	26.83	1.8×10^9	1.3×10^9
5	3.78	4.4 ± 0.4	0.200	1.44	1.63	1.10	0.021	0.134	0.079	25.87	4.4×10^9	3.2×10^9
6	5.64	5.9 ± 0.3	0.150	1.63	1.24	0.32	0.010	0.052	0.017	27.53	9.6×10^8	7.0×10^8
All	...	...	...	...	...	...	0.068	0.433	0.222	...	...	...
Q2343−BX 610												
1	4.11	4.3 ± 0.2	0.125	1.79	1.57	1.02	0.006	0.045	0.020	26.32	3.0×10^9	2.0×10^9
2	0.62	0.63 ± 0.02	0.175	1.53	1.48	0.87	0.015	0.107	0.039	25.60	5.9×10^9	3.9×10^9
3	3.16	3.5 ± 0.2	0.175	1.53	1.51	0.92	0.009	0.096	0.020	26.34	3.0×10^9	2.0×10^9
4	1.44	1.5 ± 0.1	0.125	1.79	1.43	0.77	0.007	0.059	0.018	26.45	2.7×10^9	1.8×10^9
5	4.91	5.3 ± 0.3	0.150	1.63	<1.20	...	0.005	0.043	0.009	27.23	1.3×10^9	8.8×10^8
6	1.59	2.7 ± 0.3	0.150	1.63	<1.20	...	0.004	0.063	0.005	27.93	6.9×10^8	4.6×10^8
7	3.22	3.6 ± 0.3	0.150	1.63	1.20	0.12	0.014	0.083	0.044	25.48	6.6×10^9	4.4×10^9
All	...	...	...	...	...	...	0.060	0.496	0.155	...	...	...
Q2346−BX 482												
1	4.74	4.8 ± 0.2	0.275	1.14	1.93	1.51	0.015	0.247	0.158	24.34	1.9×10^{10}	2.9×10^9
2	3.02	5.6 ± 0.9	0.150	1.63	<1.19	...	0.005	0.035	0.017	26.75	2.1×10^9	3.2×10^8
3	4.36	6.7 ± 1.3	0.175	1.53	1.83	1.39	0.007	0.060	0.018	26.71	2.2×10^9	3.3×10^8
4	1.97	2.9 ± 0.6	0.200	1.44	1.59	1.06	0.007	0.081	0.027	26.28	3.3×10^9	4.9×10^8
5	3.68	7.6 ± 1.0	0.175	1.53	1.26	0.41	0.010	0.050	0.030	26.17	3.6×10^9	5.4×10^8
All	...	...	...	...	...	...	0.045	0.473	0.250	...	...	...

Notes.

[a] Here, "clump" refers generically to $\geqslant 3\sigma$ peaks on characteristic spatial scales of 1–1.5 times the PSF FWHM above the local background in the H_{160}-band images (Section 3.1). Clumps 1 and 2 of the major merger BX 528 are part of the SE component while clump 4 is associated with the NW component. In BX 663, clump 2 is close to the center of the galaxy and may be associated with a stellar bulge or the AGN present in this object. Clump 4 of BX 389 corresponds to the small companion to the south of the main galaxy.

[b] Projected distance ($d_{\rm proj}$) relative to the geometric center of the galaxies, and deprojected distance (d) assuming a circular configuration with inclination angle corresponding to the best-fit axis ratio from the NIC2 morphology (Table 1). No projected distance is calculated for the southern companion in BX 389 (clump 4), which appears to be located below the galactic plane.

[c] Radius of the circular aperture used to measure the clump fluxes, and aperture correction based on the curve of growth from the empirical PSF light profile, corresponding to the flux ratio in circular apertures of radius 1″ and $r_{\rm phot}$.

[d] FWHM is the observed direct full-width at half-maximum from the clump radial light profiles after subtraction of the local background. FWHM^0 is the intrinsic size derived by subtracting in quadrature the observed FWHM and the PSF FWHM. For unresolved clumps, the PSF FWHM is taken as upper limit on the size.

[e] Estimates of the clump fractional contribution to the total H_{160}-band emission of the galaxies. $\mathcal{F}^{\rm cl}_{\rm PS}$ is the contribution assuming the clumps are point sources, with the local background from the host galaxy subtracted. The $\mathcal{F}^{\rm cl}_{\rm raw}$ fraction is derived from the flux in the aperture of radius $r_{\rm phot}$, without subtraction of the host galaxy background and without aperture correction. These estimates represent lower and upper limits, respectively, as argued in Section 3.1, and are listed for comparison with the adopted background-subtracted, aperture-corrected fractions simply denoted $\mathcal{F}^{\rm cl}$.

[f] Background- and aperture-corrected H_{160}-band magnitudes of the clumps (uncorrected for extinction, in the AB system).

[g] Background- and aperture-corrected equivalent rest-frame g-band luminosity of the clumps (uncorrected for extinction) relative to the Sun's g-band luminosity density (which has an absolute $M_{g,\odot} = 5.07$ mag).

[h] Stellar mass estimates for the clumps, inferred from their light contributions (background- and aperture-corrected) and the total stellar mass derived from the SED modeling of each galaxy.

using the residual maps from the Sérsic model fits (see Paper I). The light profiles extracted in circular apertures of increasing radius centered on the clump positions generally show an upturn at approximately mid-distance between bright adjacent clumps. For more isolated clumps or for those next to other comparatively fainter clumps, the profiles decrease monotonically but show a break where they become dominated by the underlying galaxy light or where the fainter neighboring clumps start to contribute more significantly. In all of those cases, we took the average brightness at the upturn or break of the profiles in annuli of width $dr = 1$–1.5 pixels to represent the local background, and computed the background-subtracted clump brightnesses within the apertures of radius $r_{\rm phot}$ just inside these annuli. For the other few clumps with no upturn or clear break in their profile, we adjusted $r_{\rm phot}$ so as to maximize the aperture size without overlapping with those of neighboring clumps, with the background also measured in narrow annuli just outside of the clump photometric apertures.

The photometric apertures have a diameter $d_{\rm phot}$ in the range $\approx(1.4$–$3.8)\times$ the PSF FWHM, on average $2\times$, and would typically miss a significant fraction of the total flux even for compact or point-like sources. Since the observed size of the clumps is comparable to the spatial resolution and their intrinsic shape is unknown, we applied a correction factor equal to the ratio of the total flux (enclosed within a radius of $1''$) and the flux within $r_{\rm phot}$ based on the PSF curve of growth. The average correction is a factor of 1.7, with a range from 1.14 to 2.09. The background measured over $r_{\rm phot} < r < r_{\rm phot} + dr$ also includes a contribution from the clump itself, which is, for the narrow annuli used, 10% on average (and in the range 4%–14%) of the total flux for a point source. This fraction is small compared with both the aperture correction and the background estimate, so we neglected this additional correction. We determined clump sizes by taking the direct FWHM of the background-subtracted light profiles (i.e., twice the radius at which the profile is half its maximum value). Nine of the 28 clumps are unresolved, with direct FWHM smaller than the PSF FWHM; we adopted the PSF FWHM as an upper limit on their size. For the others, the intrinsic FWHM size is simply calculated by subtracting in quadrature the observed clump and PSF FWHMs. The FWHM sizes, H_{160}-band magnitudes, and fractions of the total galaxy light contributed by the clumps (denoted FWHM$^{\rm cl}$, $H_{160}^{\rm cl}$, and $\mathcal{F}^{\rm cl}$) as well as the photometric aperture radii and corrections are given in Table 2.

To gauge possible uncertainties on the clump light contributions, we considered two other measurement methods. In the first, we used the peak flux above the local background as returned by *daofind* when identifying the clumps and computed the total flux assuming Gaussian unresolved sources. Since the clumps are mostly ($\sim$2/3) consistent with being extended—albeit compact—sources, this method is expected to provide lower limits. The inferred fluxes are on average (and median) a factor of $\approx$3 lower than the adopted estimates described just above, and with smaller differences typically found for the unresolved clumps (with FWHM$^{\rm cl}$ < PSF FWHM). Alternatively, we estimated the integrated light within apertures of radius $r_{\rm phot}$ but without background subtraction and aperture correction, in a manner analogous to that used by Elmegreen et al. (2009a). In view of the significant surface brightness of the underlying light in our galaxies, these estimates represent upper limits and are typically a factor $\approx$2.5 higher than the adopted values. The corresponding fractional light contributions obtained with these two approaches ($\mathcal{F}_{\rm PS}^{\rm cl}$ and $\mathcal{F}_{\rm raw}^{\rm cl}$, respectively) are also given in Table 2 for comparison with the adopted measurements. We thus infer that the adopted clump light contributions are uncertain to a factor of $\approx$3.

We emphasize that the contrast between the clumps and the surrounding, or interclump regions in the H_{160}-band images of our NIC2 targets is relatively small. In the photometric apertures employed, the total contribution from the local background light is typically $\sim$3–4 times higher than the background-subtracted clump fluxes, making the measurements of the clump brightnesses rather sensitive to the background estimates as seen above. This is very different from the "clump-cluster," "chain," and spiral galaxies from the Hubble Ultra Deep Field (H-UDF) studied in the optical by Elmegreen & Elmegreen (2005) and Elmegreen et al. (2009a), in which the clumps identified in ACS F775W imaging (i_{775} band) are typically brighter by factors of $\sim$2–4 than the surrounding emission, with the contrast increasing further at shorter wavelengths. While Elmegreen & Elmegreen (2005) accounted for the galaxy's background in measuring clump magnitudes, Elmegreen et al. (2009a) neglected this contribution since it is generally small in the optical for their sample of H-UDF galaxies.

We computed the approximate observed (i.e., uncorrected for dust extinction) rest-frame SDSS g-band luminosities of the clumps from the background-subtracted and aperture-corrected H_{160}-band magnitudes, adopting, to express the results in solar units, an absolute $M_{g,\odot} = 5.07$ mag (Blanton et al. 2001).[16] We further estimated the clump stellar masses by multiplying the $M_\star$ derived from the SED modeling of each galaxy with $\mathcal{F}^{\rm cl}$. This scaling corresponds to assuming, crudely, a constant ratio across each source between stellar mass and observed H_{160}-band light or, equivalently, rest-frame g-band light. For MD 41, the $M_\star/L_g^{\rm rest}$ ratio map obtained from the $i_{814} - H_{160}$ color map constructed from its NIC2 and ACS images indicates a fairly small scatter of $\approx$0.2 dex in observed $\log(M_\star/L_g^{\rm rest})$ across the galaxy (see Paper I). For the clumps themselves, the more detailed analysis presented in Section 4 for MD 41 and BX 482 suggests that the assumption of constant M/L ratio is on average valid to within a factor of $\sim$2–3. The clump luminosities and stellar masses, $L_g^{\rm rest,cl}$ and $M_\star^{\rm cl}$, are listed in Table 2.

3.2. Clump Properties for the NIC2 Targets

Figure 2 plots the H_{160}-band magnitude, fractional light contribution, and inferred stellar mass of the clumps as a function of observed size. The distribution of intrinsic sizes and stellar masses of the resolved clumps is shown in Figure 3. The observed FWHM sizes range from unresolved up to $\approx$2 kpc. Excluding the nine unresolved clumps, the intrinsic FWHM^0 sizes span $\approx$0.1–1.5 kpc, with mean and median of $\approx$0.9 kpc, or $\approx 0\farcs11$. The clump magnitudes vary between $H_{160,\rm AB}^{\rm cl} = 24.3$ and 27.9 mag, with mean and median of ≈ 26.5 mag. On average, the clumps have $\mathcal{F}^{\rm cl} \approx 4\%$ (median $\approx 2\%$), ranging from approximately 0.5% to 16%. With the constant M/L ratio assumption for each source, these fractions imply $M_\star^{\rm cl} \sim 9\times10^7$ to $9\times10^9\,M_\odot$, and typically $\sim10^9\,M_\odot$. Considering only the resolved clumps, the mean and median $M_\star^{\rm cl} \sim 2\times10^9\,M_\odot$. Among the resolved clumps, we find no significant correlation

[16] The NIC2 H_{160} bandpass probes a wavelength range between the rest-frame g and V bands for our targets, with closer effective wavelength and larger overlap with the g bandpass. For the best-fit SED parameters of the sources, the color term between observed g- and V-band magnitudes, or luminosities, varies from 3% to 20% depending on the object, with median/mean of $\approx$10%; the difference between the actual rest-frame luminosity probed through the H_{160} bandpass and the g band would be smaller.

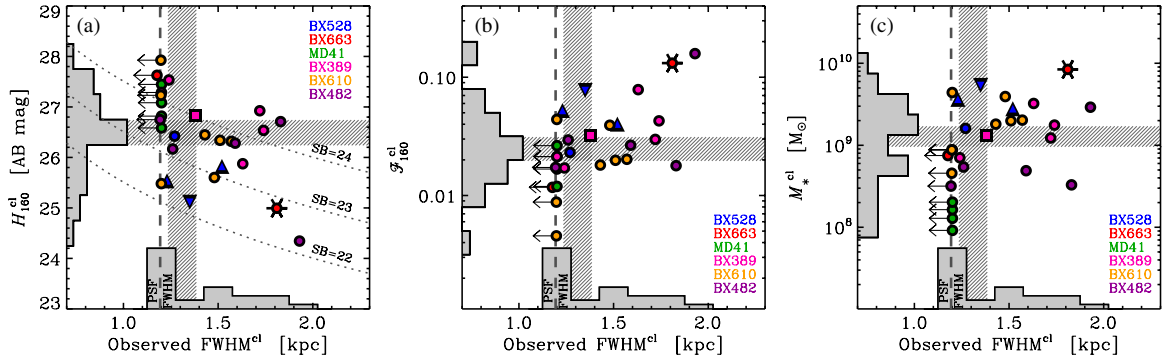

Figure 2. Properties of clumps identified in the NIC2 images of our galaxies. (a) H_{160}-band magnitude vs. observed FWHM. Dotted lines indicate curves of constant surface brightness as labeled, in units of mag arcsec^{-2}. (b) Fraction of the total galaxy H_{160}-band light measured for each clump vs. observed FWHM. (c) Derived stellar mass of the clumps vs. observed FWHM. Different colors are used for clumps belonging to different galaxies, following the scheme of the labels in each panel. Clumps associated with the southeast and northwest components of the merger system, BX 528, are plotted with triangles (upward and downward pointing, respectively), the one corresponding to the southern companion of BX 389 is plotted with a square, and the one identified as the central peak of the AGN galaxy BX 663 is marked as starred circle. In each panel, the histograms show the distributions of the measurements projected onto the horizontal and vertical axes, and the hatched bars correspond to the respective median values (including the upper limits on the observed FWHMs). The vertical dashed line shows the FWHM of the PSF. The observed FWHM of the clumps corresponds to the direct FWHM size; for unresolved clumps, the PSF FWHM is taken as an upper limit on the observed size. Magnitudes and fractional light contributions are measured in the circular apertures listed in Table 2, with the local background from the host system subtracted and an aperture correction based on the PSF profile applied, as described in Section 3.1. The stellar mass estimates are computed from the fractional light contributions assuming a constant observed $M_\star/L_{H_{160}}$ ratio across each galaxy.

(A color version of this figure is available in the online journal.)

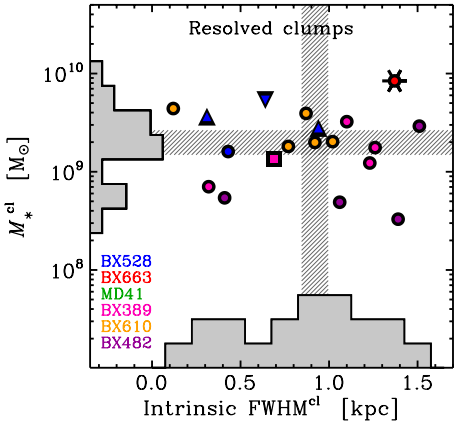

Figure 3. Stellar mass vs. intrinsic FWHM size of clumps identified in our NIC2 sample. Data are plotted only for the resolved clumps, i.e., with observed FWHM > PSF FWHM. Symbols are the same as used in Figure 2, and the histograms and hatched bars show the distributions and median values for this set of resolved clumps.

(A color version of this figure is available in the online journal.)

between clump magnitude or fractional light contribution and size, and the scatter of the data is fairly large (≈0.9 mag in H_{160}, and about equal to the mean in $\mathcal{F}^{\rm cl}$). There is also no obvious trend of clump size, magnitude, fractional light contribution, or stellar mass as a function of galactocentric distance ($d_{\rm proj}$ or d) nor of distance normalized to the $R_{\rm eff}$ of the galaxies. In Figure 2, panel (a), dotted curves indicate constant apparent central surface brightnesses, i.e., within a circular aperture of diameter equal to the observed FWHM$^{\rm cl}$. The clumps cover about 2 mag in central surface brightness, with a standard deviation of ≈0.7 mag arcsec^{-2} around the median (and mean) value of $\mu_{160,\rm AB} \approx 23.7$ mag arcsec^{-2}. This value corresponds roughly to the 3σ surface brightness limit of our NIC2 images.

The "clumps" associated with the merger components of BX 528, the southern companion of BX 389, and the central core of BX 663 (plotted with different symbols in Figures 2 and 3) do not differentiate in terms of size but are part of the brighter half and have $\mathcal{F}^{\rm cl}$ above the median value. Excluding them from our clump sample does not, however, significantly affect the ranges and the mean or median properties inferred above nor the absence of correlation between clump properties.

Despite being a striking feature in the appearance of all our targets, our results imply that the individual clumps contribute typically only a few percent of the total light. Even with the substantial uncertainties of a factor of ≈3, each clump still represents a fairly small contribution. Summed up over all clumps identified in a given galaxy, the total contributions are typically ∼15% per object, ranging from roughly 10% to 25% (at least ∼5% from the lower limits obtained in the alternative "point-source" estimates made above, and at most ∼50% from the upper limits derived without subtracting the host background in the photometric apertures). Thus, for our targets, the bulk of the rest-frame ≈5000 Å light appears to be dominated by an underlying component from a more smoothly distributed stellar population. Alternatively, fainter, unresolved clumps and clusters may also contribute to this extended emission component.

We searched for correlations between clump properties and the global properties derived from the SED modeling of the host source. There is no significant correlation between clump size, magnitude, or fractional light contribution with galaxy stellar mass, age, absolute and specific SFR, nor between clump size and fractional light contribution and extinction. The only possible trend is of fainter clump H_{160}-band magnitude with higher A_V, with Spearman's rank correlation coefficient $\rho = 0.53$ and 2.8σ significance level.[17] The trend weakens when excluding the clumps associated with the merging components of BX 528, the southern companion of BX 389, and the central peak of the AGN source BX 663 ($\rho = 0.37$, 1.7σ). There is no apparent trend with morphological parameters although it is noteworthy that BX 610 and BX 482, the two disks with qualitatively most prominent clumps, have higher Gini coefficients than MD 41 and BX 389, the two disks where the clumps appear visually less regular in shape. MD 41 and BX 389

[17] The significance quoted corresponds to the number of standard deviations by which the sum-squared difference of ranks deviates from the expected value under the null hypothesis of statistical independence ($\rho = 0$).

are the most edge-on disks based on their axis ratio and have the largest inferred A_V, such that higher and possibly patchy extinction may affect the appearance of these galaxies more than for the others. Our sample is small, however, and covers a limited range in host galaxy parameters (Section 2.2), therefore it would be difficult to discern all but the strongest possible trends.

3.3. Constraints on Emission Line Contributions

At the redshift of our targets, the NIC2 F160W bandpass includes the [O III] $\lambda\lambda$ 4959, 5007 doublet and Hβ. It is thus important to assess whether the observed H_{160}-band morphologies are biased by nebular line emission. For all sources except BX 528, SINFONI seeing-limited observations of these lines with the H-band grating were taken as part of the SINS survey (Förster Schreiber et al. 2009), and are analyzed in detail by P. Buschkamp et al. (2011, in preparation). The [O III] lines are detected in all galaxies except BX 663, and Hβ is additionally detected in MD 41 and BX 610. Some of the non-detections can be attributed to the galaxies' lines being redshifted to the wavelength of bright telluric lines, in particular Hβ for BX 663 and BX 482. Based on the integrated line fluxes (or the 3σ upper limits thereof), we concluded in Paper I that the broadband H_{160} emission of our NIC2 targets is dominated by the continuum, with only a modest to very small fraction from the [O III] and Hβ lines. The largest line contribution is inferred for BX 389, where the [O III] lines make up 24% of the integrated H_{160}-band flux and, with the 3σ upper limit on Hβ, the total line contribution is estimated at <29%. BX 610 has the smallest contributions, amounting to ≈6% for all three lines combined. Our examination of the sources on a pixel-to-pixel basis further indicates no important spatial variations in the emission line contributions.

In the context of this paper, it is worth considering more specifically whether the clumps identified in Section 3.1 could be due to nebular line emission rather than stellar continuum emission, because their contribution also represents a modest fraction of the total H_{160}-band light. A detailed assessment would require AO-assisted SINFONI H-band observations, but the existing seeing-limited data provide useful indications. For BX 610 and BX 482, the total fraction of light from the identified clumps (16% and 25%, respectively; Table 2) is at least twice as high as the total emission line contribution (6% and <12%; Paper I), implying a major contribution from the continuum in these two sources. For BX 663, MD 41, and BX 389, the line contributions (or 3σ upper limits thereof) are comparable to or higher than the sum of the clump contributions such that it is not possible to set the same constraints with the current data. For BX 482, the spatial distributions in Hα and H_{160} band follow each other fairly well, albeit with some small differences discussed in the next section. Our analysis in Section 4 implies that the Hα to H_{160}-band flux ratio at the location of the clumps identified in the NIC2 image is a factor of $\lesssim$2 the source-integrated ratio. If we assume approximately constant observed emission line ratios across the galaxy, this would imply [O III] and Hβ contributions to the H_{160}-band emission of at most twice that of the global contribution, i.e., $\lesssim$25% (Paper I). Again, this means that the clumps need to have a major component of continuum light in H_{160} band. From the estimates above, and at least for BX 610 and BX 482, the clumps in the NIC2 images do not appear to be predominantly caused by line emission. More generally, clumps identified in high-resolution optical and near-IR broadband imaging of other samples (e.g., Elmegreen & Elmegreen 2005; Elmegreen et al. 2009a) are ubiquitous in $z \gtrsim 1$ galaxies, over a range of redshift that precludes an origin entirely from emission lines in all cases.

4. DETAILED CASE STUDIES: MD 41 AND BX 482

The sizes, luminosities, and stellar masses derived in the previous section reflect the current state of the clumps but provide little information on their evolution. In addition, the stellar masses were based on the crude assumption of constant M/L ratio across the galaxies. In the following, we examine two of our targets with existing high spatial resolution ancillary data to assess possible variations in M/L ratios and search for differences in age-sensitive properties among clumps, and between clump and interclump regions. We combine our NIC2 maps with the available ACS imaging for MD 41 to look at the $i_{814} - H_{160}$ colors, and with the AO-assisted SINFONI Hα map of BX 482 to determine the Hα equivalent widths. As we will see, the $i_{814} - H_{160}$ colors provide notably tighter constraints on the M/L ratios, irrespective of dust extinction, stellar age, and SFH. On the other hand, the Hα equivalent widths are insensitive to extinction if the line and continuum emission originates from the same regions, and are thus most useful to constrain variations in stellar ages.

4.1. MD 41: Constraints from NIC2 and ACS Observations

4.1.1. Rest-frame Optical- and UV-identified Clumps

The ACS i_{814}-band map of MD 41 is shown in Figure 4 alongside the NIC2 H_{160}-band map and a color-composite image. For the analysis, the ACS map has been convolved to the spatial resolution of the NIC2 data and registered onto the same astrometric frame (see Paper I for details). The appearance of MD 41 is broadly similar in i_{814} and H_{160} band. The measurements in Paper I of the structural and morphological parameters yield comparable effective radius, Sérsic n index, axis ratio, as well as Gini G, Multiplicity Ψ, and M_{20} coefficients for both images. The $i_{814} - H_{160}$ colors across MD 41 are also fairly uniform, with median of 0.95 mag and standard deviation of 0.37 mag over the regions where pixels have S/N > 3 in both bands. These results indicate that there is no strong k-correction between the rest-frame UV and optical morphologies for MD 41, consistent with the general findings for rest-UV-selected samples at $z \sim 2$, and in contrast to those for samples selected at longer wavelengths with typically redder rest-frame optical colors (Peter et al. 2007; Law et al. 2007; Toft et al. 2007; Cameron et al. 2010).

However, it is also evident from Figure 4 that the brightest peaks do not all coincide spatially between the two maps. Therefore, we applied the procedure described in Section 3.1 to detect clumps in the ACS image matched to the PSF of the NIC2 data, using the same detection parameters in the IRAF task *daophot*. Four clumps are thus identified in i_{814}-band emission, one of which corresponds to NIC2 clump 4 whereas the three others have no counterpart among the NIC2 clumps (hereafter referred to as "ACS-1," "ACS-2," and "ACS-3"). All of the clumps are indicated on the maps of Figure 4. We computed the clump photometry with background subtraction and aperture correction, as well as without for comparison purposes (hereafter simply "background-subtracted" and "raw" photometry). We measured the i_{814}-band brightness of the NIC2 clumps in the same apertures used to derive their H_{160}-band brightnesses. For the three additional ACS clumps, we defined appropriate apertures as explained in Section 3.1 but based on the i_{814}-band light profiles. The ACS-only clumps have

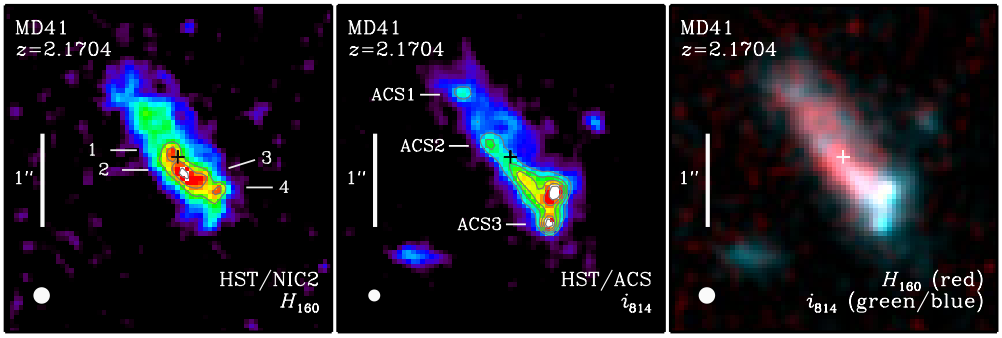

Figure 4. Comparison of rest-frame optical and UV morphologies for MD 41. North is up and east to the left in both images, and a bar of 1″ in length indicates the scale in the images. Left: NIC2 H_{160}-band map, with the FWHM = 0.″145 of the PSF indicated by the filled circle at the bottom left corner. Middle: the same as the left panel but for the ACS i_{814}-band map, at the original resolution of the data with PSF FWHM = 0.″099. Right: color composite after accurate PSF matching and registration of the NIC2 and ACS maps; in this RGB image, the red channel is assigned to the H_{160} band, and the green and blue channels to the i_{814} band. The colors for all images plotted correspond to a linear flux density scale. The white cross shows the location of the geometric center of MD 41 as determined from the NIC2 map. Overall, the images are strikingly similar, although on small scales there are noticeable differences. In particular, the two brightest clumps in the ACS image on the southwest edge of the galaxy are much fainter in the NIC2 image and, consequently, have bluer colors than the bulk of the source. Clumps identified in the NIC2 H_{160}-band image are labeled in the left panel, and those identified in the ACS i_{814}-band map that have no counterpart in H_{160}-band emission are labeled in the middle panel.

(A color version of this figure is available in the online journal.)

Table 3
H_{160}- and i_{814}-band Magnitudes and Color-based Properties of Clumps Identified in the NIC2 and ACS Images of MD 41

Clump	$d_{\rm proj}$[a]	d[a]	$r_{\rm phot}$[b]	From "Raw" Photometry[c]				From Background-subtracted Photometry[d]			
				$H_{160}^{\rm cl}$	$i_{814}^{\rm cl}$	$\log(M_\star/L_g^{\rm rest,\,cl})$	$M_\star^{\rm cl}$	$H_{160}^{\rm cl}$	$i_{814}^{\rm cl}$	$\log(M_\star/L_g^{\rm rest,\,cl})$	$M_\star^{\rm cl}$
	(kpc)	(kpc)	(arcsec)	(mag)	(mag)	($\log[M_\odot\,L_{\odot,\,g}^{-1}]$)	($10^8\,M_\odot$)	(mag)	(mag)	($\log[M_\odot\,L_{\odot,\,g}^{-1}]$)	($10^8\,M_\odot$)
1	0.56	1.1 ± 0.2	0.10	26.20 ± 0.04	27.45 ± 0.02	$-0.71^{+0.18}_{-0.17}$	$6.4^{+3.3}_{-2.1}$	27.08 ± 0.21	>29.65	>-0.15	>10.0
2	1.65	2.3 ± 0.2	0.10	26.03 ± 0.04	27.16 ± 0.02	$-0.75^{+0.17}_{-0.16}$	$6.8^{+3.2}_{-2.1}$	26.82 ± 0.17	28.23 ± 0.10	$-0.65^{+0.27}_{-0.23}$	$4.2^{+3.6}_{-1.8}$
3	2.96	3.2 ± 0.1	0.10	26.16 ± 0.04	27.03 ± 0.02	-0.89 ± 0.17	$4.4^{+2.1}_{-1.4}$	27.45 ± 0.30	28.84 ± 0.17	$-0.65^{+0.35}_{-0.27}$	$2.3^{+2.9}_{-1.3}$
4	4.77	5.8 ± 0.4	0.10	26.26 ± 0.05	26.68 ± 0.01	-1.15 ± 0.17	$2.2^{+1.1}_{-0.7}$	26.59 ± 0.13	27.77 ± 0.06	$-0.73^{+0.22}_{-0.20}$	$4.3^{+2.9}_{-1.7}$
ACS-1	6.95	7.0 ± 0.1	0.10	27.16 ± 0.11	27.62 ± 0.03	$-1.13^{+0.22}_{-0.20}$	$1.0^{+0.7}_{-0.4}$	>27.67	28.64 ± 0.14	<-0.84	<1.2
ACS-2	1.91	2.9 ± 0.4	0.10	26.73 ± 0.07	27.37 ± 0.02	-1.02 ± 0.19	$1.9^{+1.1}_{-0.7}$	>27.67	28.53 ± 0.13	<-0.90	<1.1
ACS-3	6.89	7.3 ± 0.2	0.15	26.46 ± 0.09	26.21 ± 0.01	-1.61 ± 0.18	$0.64^{+0.33}_{-0.22}$	>27.49	26.78 ± 0.03	<-1.95	<0.11

Notes. H_{160} and i_{814} photometry and color-based properties of clumps in MD 41, where the set of four clumps identified in the NIC2 image (1 to 4) is augmented with three clumps identified in the ACS map but not in the NIC2 map (see Figure 4). The ratio of stellar mass to rest-frame g-band luminosity (uncorrected for extinction) of the clumps is computed from the relationship between observed $i_{814} - H_{160}$ color and $M_\star/L_g^{\rm rest}$ derived in Paper I (see also Section 4.1). The clump stellar masses listed here are obtained from the color-based $M_\star/L_g^{\rm rest}$ ratios inferred for individual clumps instead of being based on a uniform ratio across the galaxy as implicitly assumed for the estimates reported in Table 2.

[a] Projected distance ($d_{\rm proj}$) relative to the geometric center of the galaxies, and deprojected distance (d) assuming the clumps lie in a disk of inclination with respect to the sky plane given by the morphological axis ratio (Table 1).

[b] Radius of the circular aperture used to measure the clump fluxes.

[c] Properties based on the fluxes measured in the circular aperture of radius $r_{\rm phot}$, without subtraction of the local background from the galaxy and without aperture correction. The 1σ photometric uncertainties are computed from the noise properties of the images. The uncertainties for the $M_\star/L_g^{\rm rest}$ and $M_\star$ results account for those of the magnitudes and the accuracy of the $i_{814} - H_{160}$ versus $M_\star/L_g^{\rm rest}$ relationship (≈0.15 dex; see Section 4.1.3).

[d] Properties based on the fluxes measured in the circular aperture of radius $r_{\rm phot}$ with local background subtraction and aperture correction. For $r_{\rm phot} = 0.''10$ and $0.''15$, the aperture correction is a factor of 2.09 and 1.63, respectively. The 1σ photometric uncertainties reflect the noise properties of the images and account for both the measurement of clump and background fluxes; 3σ limits are given for clumps with background-subtracted fluxes in one or the other band that are smaller than the 3σ photometric uncertainty. The uncertainties for the $M_\star/L_g^{\rm rest}$ and $M_\star$ results are obtained in the same way as for those based on the raw photometry.

no local excess emission above our detection threshold in the NIC2 map, so we adopted 3σ upper limits on their background-subtracted H_{160}-band magnitudes based on the noise properties of the image. For the NIC2-identified clumps, the background-subtracted i_{814}-band magnitudes are formally above the 3σ noise level in the photometric apertures except for clump 1, for which we used a 3σ upper limit.

4.1.2. Variations in Colors of the Clumps

The photometric measurements are reported in Table 3 and plotted in Figure 5. Panel (a) shows the H_{160}- versus i_{814}-band magnitudes for individual pixels with S/N > 3 in each band. Panel (b) shows the magnitudes estimated for the clumps, with and without subtraction of the galaxy's background. For reference, the total magnitudes of MD 41 (in a circular aperture of 3″ diameter) and those corresponding to the sum of the fluxes of all pixels with S/N > 3 in both bands are shown as well .[18] In both panels of Figure 5, the diagonal lines correspond to constant $i_{814} - H_{160}$ colors. A vector shows the significant impact of extinction in the rest frame of the galaxy on the observed colors.

[18] The small difference between these two "integrated" measurements is due to the different areas sampled, with the total aperture including the two sources ∼1″ southeast and northwest of MD 41 seen in the ACS image but undetected in the NIC2 image.

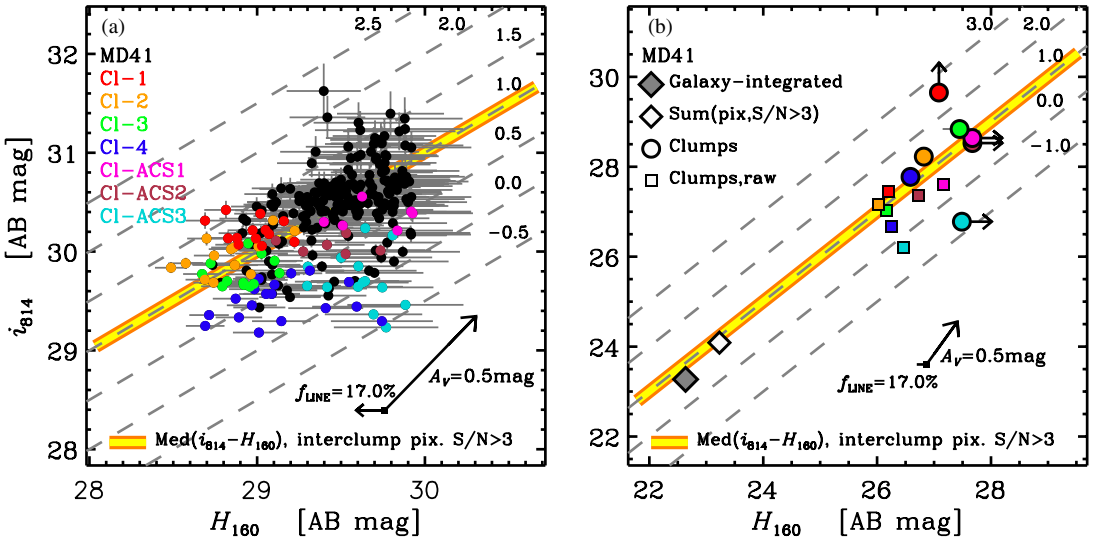

Figure 5. Observed near-IR H_{160}-band and optical i_{814}-band magnitudes from the *HST* ACS and NIC2 imaging of MD 41. (a) Data for all individual pixels across MD 41 with an S/N > 3 in both H_{160} and i_{814} bands. Error bars correspond to 1σ uncertainties on the measurements. Pixels that fall within the photometric apertures of different clumps are color-coded according to the scheme given by the labels. Black data points show pixels in the interclump regions. Diagonal dashed lines correspond to constant $i_{814} - H_{160}$ colors, as labeled in the plot; the thick yellow–orange line shows the median color of pixels in the interclump regions. The arrows indicate the effects of $A_V = 0.5$ mag of extinction on the magnitudes, and of an emission line contribution in the H_{160} bandpass of 17% derived from the integrated [O III] $\lambda\lambda$4959, 5007 and Hβ line fluxes for MD 41 measured with SINFONI. (b) The same as panel (a) but for the clump magnitudes. Results based on the "background-subtracted" and "raw" photometry (as explained in Section 4.1.1) are plotted as circles and squares, respectively. Error bars (mostly smaller than the symbol size) correspond to the formal photometric uncertainties. For clumps undetected in one or the other band, 3σ upper limits on their background-subtracted photometry are used. For comparison, the integrated magnitudes of MD 41 and those obtained by summing up the fluxes of all individual pixels with S/N > 3 are plotted as gray and white filled diamonds, respectively. The variations in colors across MD 41 and among the clumps are fairly modest for the most part; NIC2 clump 1 and clump ACS-3 exhibit the most significant differences. The NIC2-identified clumps tend to be redder than those identified only in the ACS image.

(A color version of this figure is available in the online journal.)

All the NIC2 and ACS clumps in MD 41 contribute small fractions of ∼1%–5% to the galaxy-integrated fluxes in both H_{160} and i_{814}-band emission (rest frame ≈5000 Å and ≈2600 Å), respectively. Overall, the clump and interclump regions in MD 41 span a comparable range in their colors, reflecting the uniformity across the galaxy noted above. The median color of the interclump regions is 1.0 mag, nearly equal to the median over all S/N > 3 pixels (0.95 mag). The colors of the clumps are mostly within ≈0.5 mag of these values, for both the raw and background-subtracted estimates (or limits). Interestingly, there appears to be a systematic difference in colors between the clumps identified in the different bands: the NIC2 clumps have a median color roughly 0.6 mag redder than the ACS clumps. The two most distinct clumps are NIC2-1 and ACS-3, which have colors up to 2 mag redder and bluer, respectively, than the ensemble of the other clumps and the interclump regions.

4.1.3. Implications for the Stellar Properties of the Clumps

With the $i_{814} - H_{160}$ colors of the clumps in MD 41, we can assess the reliability of the assumption made in Section 3.1 on their M/L ratio and the consequences on the clump stellar masses. To interpret the colors, we used the mean $i_{814} - H_{160}$ versus $M_\star/L_g^{\rm rest}$ relationship derived in Paper I from the evolutionary synthesis models of Bruzual & Charlot (2003) for a wide range of SFHs, stellar ages, and dust extinction. The observed $i_{814} - H_{160}$ colors are strongly degenerate in age, extinction, and SFH. On the other hand, the various model curves occupy a fairly well-defined locus in the $i_{814} - H_{160}$ versus $M_\star/L_g^{\rm rest}$ parameter space, and the standard deviation of the models suggest that the relation is accurate to 0.15 dex in $\log(M_\star/L_g^{\rm rest})$ over the range of colors observed across MD 41, with little sensitivity to metallicity between solar and 1/5 solar (appropriate for our NIC2 targets including MD 41; P. Buschkamp et al. 2011, in preparation). Stellar masses were then estimated by multiplying the M/L ratios with the observed luminosities from the H_{160}-band data. The color-based $M_\star/L_g^{\rm rest}$ and $M_\star$ estimates for all clumps identified in MD 41 are given in Table 3.

The color distribution of individual pixels across MD 41 implies a median $\log(M_\star/L_g^{\rm rest}\,[M_\odot\,L_{\odot,g}^{-1}]) \approx -0.8$ over the interclump regions (−0.85 over all S/N > 3 pixels). For most clumps, the ratios (or limits thereof) derived from the colors agree within a factor of ∼2–3 with the median over the interclump regions. The most notable differences are for the reddest and bluest clumps, NIC2-1 and ACS-3. The ratio between the $M_\star/L_g^{\rm rest}$ values (or limits thereof) for these two clumps ranges from ≈8 to 65, depending on the treatment of the galaxy's background. The systematic offset in colors between the NIC2- and ACS-identified clumps implies overall higher $M_\star/L_g^{\rm rest}$ ratios and larger $M_\star$ for the former set of clumps by factors of ∼2 and ∼4–6, respectively (or more considering the limits). For the NIC2-identified clumps 2, 3, and 4, the background-subtracted color-based masses inferred here are ≈1.5–2.5 times larger than those calculated in Section 3.1 with the assumption that clumps have the same M/L ratio as the entire galaxy; for clump 1, it is almost a factor of eight higher. The comparison of the trends based on the raw versus background-subtracted photometry in MD 41 indicates that, while still fairly modest between most clumps, the variations in colors, and hence M/L ratios, tend to be accentuated (along with a general shift toward redder colors and higher M/L ratios) when accounting for the galaxy's background light contribution.

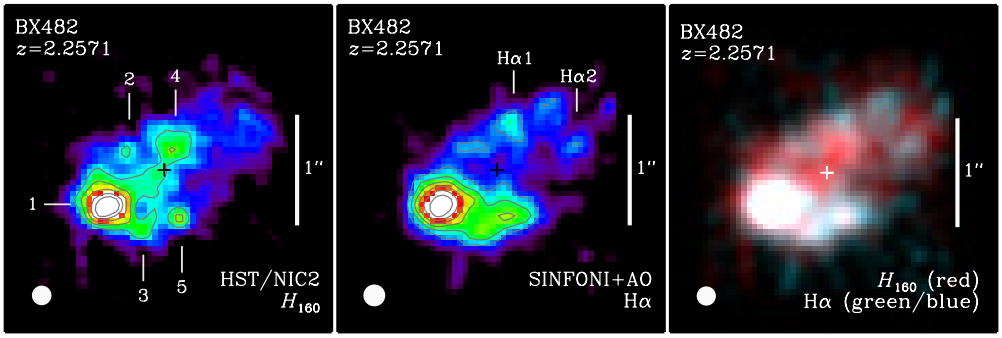

Figure 6. Comparison of Hα and rest-frame optical morphologies for BX 482. North is up and east to the left in both images, and a bar of 1″ in length indicates the scale in the images. Left: NIC2 H_{160}-band image at the original angular resolution of the data, with the FWHM = 0.″145 of the PSF indicated by the filled circle at the bottom left corner. Middle: the same as the left panel but for the SINFONI Hα map, with PSF FWHM = 0.″17. Right: color composite after accurate PSF matching and registration of the NIC2 and Hα maps; in this RGB image, the red channel is assigned to the H_{160} band and the green and blue channels to Hα. The colors for all images plotted correspond to a linear flux density scale. The white cross shows the location of the geometric center of BX 482 as determined from the NIC2 map. The H_{160} band and Hα emission follow each other closely although on small spatial scales there are some noticeable differences. In particular, the clumpy structure on the northwestern side of the galaxy center has less correspondence between the two maps than on the southeastern side. Clumps identified in the NIC2 H_{160}-band image are labeled in the left panel, and those identified in the SINFONI Hα line map that have no counterpart in H_{160}-band emission are labeled in the middle panel.
(A color version of this figure is available in the online journal.)

The observed distributions of colors in MD 41 could be interpreted as indicative of overall modest variations in extinction and ages between clumps and across the galaxy, with the apparent exceptions of NIC2-1 and ACS-3. The difference in median $i_{814} - H_{160}$ color between the NIC2- and ACS-identified clumps by 0.6 mag could be accounted for by a difference in A_V of about 0.7 mag. Relative to the interclump regions, the redder color of NIC2-1 and bluer color of ACS-3 by up to ≈2 mag would require differences in A_V of up to about 2.5 mag; given the best-fit $A_V = 1.2$ mag for the integrated SED of MD 41 (Table 1), it appears plausible that not only extinction but also age variations contribute to the observed clump colors, at least for these two clumps. If interpreted solely in terms of stellar age, assuming CSF and a uniform $A_V = 1.2$ mag, the NIC2-only clumps would be on average ∼5–10 times older than the ACS-only clumps. Shorter timescales for the star formation activity would tend to reduce (but not eliminate) the overall relative age difference between NIC2- and ACS-only clumps, if extinction variations are neglected.

The results for MD 41 suggest that, with the possible exception of the reddest and bluest clumps, the M/L and stellar masses are reliable to a factor of a few. The NIC2-identified clumps tend to be redder and more massive than the ACS-identified clumps. We find indications that not only extinction effects but also variations in stellar age are likely responsible for the full range in colors of the clumps. The main uncertainties affecting our analysis are associated with the limited photometry available for MD 41 and with the difficulties in evaluating the clump light in the presence of a bright background from the host galaxy.

4.2. BX 482: Constraints from NIC2 and SINFONI Observations

4.2.1. Rest-frame Optical- and Hα-identified Clumps

For BX 482, we can set more robust constraints on relative stellar ages between the clumps and the interclump regions with the help of the SINFONI AO-assisted Hα map available for this galaxy. Ideally, the Hα line flux combined with the continuum emission measured in the near vicinity of Hα in wavelength would provide the Hα equivalent width, which varies strongly with the age of a stellar population but is insensitive to dust extinction.[19] However, the continuum map from our SINFONI data of BX 482 has insufficient S/N for our purposes, so we used the H_{160} map as a proxy. In what follows below, the Hα equivalent widths are calculated in the rest frame (denoted $W^{\rm rest}$(Hα)) assuming a flat f_ν continuum flux per unit frequency between rest-frame 5000 Å and 6563 Å and using the wavelength of Hα for the conversion to continuum flux per unit wavelength, f_λ.

We analyzed the NIC2 H_{160} and SINFONI Hα data of BX 482 in the same fashion as the NIC2 and ACS data of MD 41, matching the NIC2 PSF to that of the SINFONI data, which has an FWHM = 0.″17. The NIC2 and Hα images were aligned relying primarily on the outer isophotes and on the brightest clump visible in both maps (NIC2-1). We refer the reader to Paper I for a full description of these procedures. The NIC2 H_{160}-band and SINFONI Hα maps are shown in Figure 6 along with a color-composite image created from the PSF-matched maps. Both the lower-surface-brightness component and the brighter substructure are overall very comparable between the H_{160} band and Hα emission. This similarity is reflected in the nearly equal values of G, Ψ, and M_{20} coefficients, and the structural parameters $R_{\rm eff}$, n, and b/a from both images agree well within the 1σ uncertainties (see Paper I).

However, some differences do exist in the details of the spatial distributions. Specifically, clump 4 identified in the NIC2 data does not have an obvious counterpart in Hα, whereas there are peaks in Hα, significantly offset to the north of clump 4 and on the northwestern side, that are not apparent in the NIC2 image. We thus ran the clump detection procedure on the Hα map, finding matches for all NIC2 clumps except 4, and two additional clumps in line emission, hereafter denoted "Hα-1" and "Hα-2." The clumps are indicated on the maps of Figure 6. We measured the H_{160} band and Hα fluxes of each clump, within the same aperture for consistent photometry, and both with and without

[19] This statement is true unless different amounts of dust obscure the H II regions compared to the bulk of the stellar population, or a significant fraction of Lyman continuum photons is absorbed by dust within the H II regions or escapes from the H II regions. In the analysis presented here, we neglected these effects. There is evidence for such "differential attenuation" on global galactic scales locally (e.g., Calzetti et al. 2000) and at high-z (e.g., Förster Schreiber et al. 2009; Mancini et al. 2011; Yoshikawa et al. 2011), but if it is similar at different locations across galaxies, the *relative* age estimates would not be significantly affected.

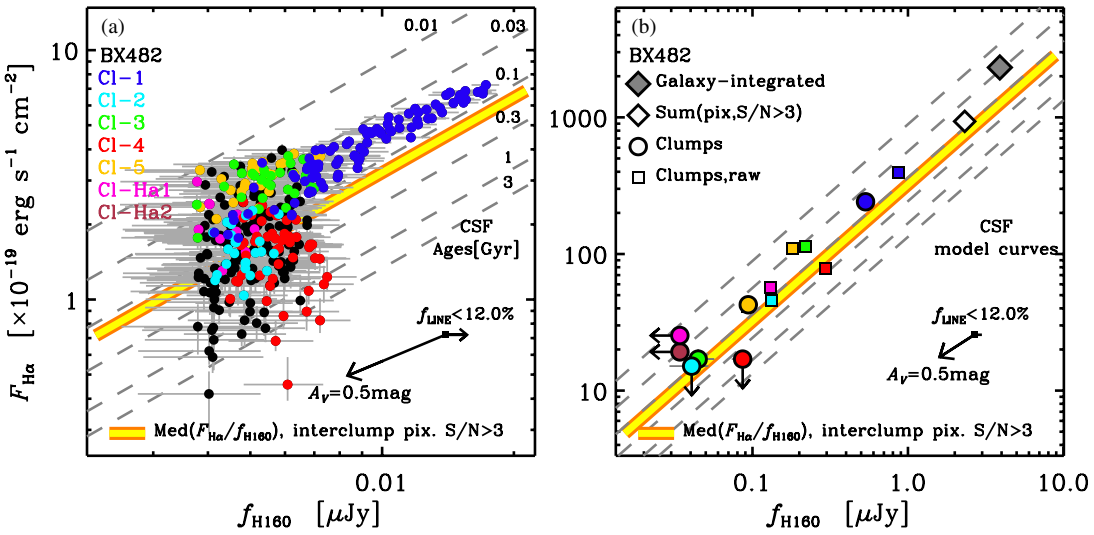

Figure 7. Observed near-IR H_{160} flux density and Hα line flux from the *HST* NIC2 imaging and SINFONI + AO observations of BX 482. (a) Data for all individual pixels across BX 482 with an S/N > 3 in both H_{160} band and Hα emission. Error bars show the 1σ uncertainties on the measurements. Pixels that fall within the photometric apertures of different clumps are color-coded according to the scheme given by the labels, and black data points show pixels in the interclump regions. Diagonal dashed lines correspond to constant rest-frame Hα equivalent widths, translated to stellar ages based on model predictions for constant star formation (see Section 4.2.3 for details); ages in Gyr are labeled next to each line (and, from young to old ages, correspond to $W^{\rm rest}$(Hα) = 415, 265, 170, 115, 80, and 60 Å). The thick yellow–orange line shows the median age inferred for pixels in the interclump regions. The arrows indicate the effects of $A_V = 0.5$ mag of extinction on the fluxes, and of the upper limit for the contribution in the H_{160} bandpass of 12% derived from the integrated fluxes of the [O III] $\lambda\lambda$4959, 5007 emission lines and the 3σ limit for Hβ measured in BX 482 with SINFONI. (b) The same as panel (a) but for the clump measurements. Results based on the "background-subtracted" and "raw" photometry (as explained in Section 4.2.1) are plotted as circles and squares, respectively. Error bars (mostly smaller than the symbol size) correspond to the formal photometric uncertainties. For clumps undetected in one or the other image, 3σ upper limits on their background-subtracted photometry are used. The integrated fluxes for BX 482 and those summed up over all individual pixels with S/N > 3 are plotted as gray and white filled diamonds, respectively. The model curves are for the same ages as in panel (a). The clumps span a comparable range in $W^{\rm rest}$(Hα), hence in inferred stellar ages, as the interclump regions. The NIC2-identified clumps tend to have lower ratios, suggesting older ages, than those identified only in the Hα map.

(A color version of this figure is available in the online journal.)

subtraction of the galaxy's background. An aperture correction was applied for the background-subtracted measurements. The same apertures as in Section 3.1 were used for the NIC2-identified clumps (the H_{160}-band magnitudes measured from the original and PSF-matched NIC2 maps are not significantly different). For the Hα-only clumps, the apertures were chosen based on the Hα light profiles. For clumps undetected in one or the other map, we adopted 3σ upper limits on their background-subtracted fluxes, derived from the noise properties of the images. The flux measurements are given in Table 4.

4.2.2. Variations in Hα Equivalent Width of the Clumps

Figure 7 shows in panel (a) the distribution of H_{160}-band flux densities versus Hα line fluxes for individual pixels with S/N > 3 in each map. In panel (b), the results for the clumps (with and without background subtraction) are plotted along with the galaxy-integrated measurements and the fluxes summed over S/N > 3 pixels for comparison.[20] Diagonal lines are overplotted in both panels, corresponding to constant values of $W^{\rm rest}$(Hα) and labeled with equivalent stellar ages for CSF models as described below. Extinction does not have a significant effect on the $W^{\rm rest}$(Hα) due to the proximity in wavelength of Hα and the rest-frame ≈5000 Å region probed by the H_{160} bandpass; the effects of extinction run nearly parallel to the lines of constant Hα equivalent width in Figure 7.

Most clumps in BX 482 contribute ∼1%–5% of the total emission in both H_{160} band and Hα, and the clumps and interclump regions span a comparable range of Hα equivalent widths. While there are some differences for individual clumps between the background-subtracted and raw flux estimates, the median properties are almost the same. In the ensemble, the clumps have higher $W^{\rm rest}$(Hα) than the interclump regions, with median values of 210 Å and 150 Å, respectively. The two Hα-identified clumps have the highest background-subtracted equivalent widths. Two clumps are of particular interest in BX 482: NIC2 clumps 1 and 4. Clump 1 is the largest, most luminous, and one of the most massive of all clumps identified in our NIC2 targets (see Section 3.2). It also has the largest contribution to the total host galaxy's emission, ∼15% in H_{160} band as well as in Hα, roughly (5–10) × higher than the average clump in our NIC2 targets. However, clump 1 does not differentiate in terms of its $W^{\rm rest}$(Hα), which is equal to the median value of all clumps in BX 482. In contrast, clump 4 has about the same size and fractional light contribution as the median values for the clumps in our NIC2 targets, but it is one of the least massive clump. It is further distinct among the BX 482 clumps, with the lowest measured $W^{\rm rest}$(Hα) ∼ 90–120 Å, depending on whether the galaxy background is subtracted or not.

4.2.3. Variations in Ages of the Clumps and Implications for the M/L Ratios

To interpret the Hα equivalent widths in terms of stellar ages, we computed model predictions using the Bruzual & Charlot (2003) evolutionary synthesis code with a Chabrier (2003) IMF and solar metallicity. The Hα flux was calculated from the H ionizing rates of the models, applying the recombination coefficients for case B from Hummer & Storey (1987) for an electron temperature $T_e = 10^4$ K and density $n_e = 10^3$ cm^{-3} (see, e.g., Förster Schreiber et al. 2009), and the H_{160}-band flux

[20] The small differences between the latter two are due to fewer pixels meeting the S/N criterion on the fainter northwest side than on the southeast side within the radius of 1.″5 of the total photometric aperture.

Table 4
H_{160}-band Magnitudes, Hα Fluxes, and Stellar Ages of Clumps Identified in the NIC2 and SINFONI Maps of BX 482

Clump	$d_{\rm proj}$[a]	d[a]	$r_{\rm phot}$[b]	From "Raw" Photometry[c]			From Background-subtracted Photometry[d]		
				$H_{160}^{\rm cl}$	$F_{\rm H\alpha}^{\rm cl}$	Age	$H_{160}^{\rm cl}$	$F_{\rm H\alpha}^{\rm cl}$	Age
	(kpc)	(kpc)	(arcsec)	(mag)	(10^{-17} erg s^{-1} cm^{-2})	(Myr)	(mag)	(10^{-17} erg s^{-1} cm^{-2})	(Myr)
1	4.74	4.8 ± 0.2	0.275	23.97 ± 0.02	3.92 ± 0.05	55 ± 3	24.50 ± 0.03	2.41 ± 0.05	55^{+6}_{-5}
2	3.02	5.6 ± 0.9	0.15	26.02 ± 0.05	0.46 ± 0.03	115^{+26}_{-20}	27.30 ± 0.30	<0.15	>94
3	4.36	6.7 ± 1.3	0.175	25.47 ± 0.04	1.14 ± 0.03	37^{+5}_{-4}	27.19 ± 0.29	0.17 ± 0.03	88^{+170}_{-47}
4	1.97	2.9 ± 0.6	0.20	25.14 ± 0.03	0.78 ± 0.04	239^{+40}_{-33}	26.48 ± 0.16	<0.17	>570
5	3.68	7.6 ± 1.0	0.175	25.68 ± 0.04	1.09 ± 0.03	25^{+4}_{-3}	26.39 ± 0.14	0.43 ± 0.03	54^{+30}_{-17}
Hα-1	3.69	5.8 ± 1.1	0.15	26.03 ± 0.05	0.57 ± 0.03	60^{+12}_{-10}	>27.49	0.25 ± 0.03	<15
Hα-2	6.31	6.6 ± 0.8	0.15	26.41 ± 0.07	0.42 ± 0.03	56^{+16}_{-12}	>27.49	0.19 ± 0.03	<30

Notes. H_{160}-band and Hα photometry and stellar age of clumps in BX 482, where the set of five clumps identified in the NIC2 image (1 to 5) is augmented with two clumps identified in the SINFONI Hα map but not in the NIC2 map (see Figure 6). The stellar age is inferred from the rest-frame Hα equivalent width using Bruzual & Charlot (2003) evolutionary synthesis models for a constant star formation rate, as described in Section 4.2.

[a] Projected distance ($d_{\rm proj}$) relative to the geometric center of the galaxies, and deprojected distance (d) assuming the clumps lie in a disk of inclination with respect to the sky plane given by the morphological axis ratio (Table 1).

[b] Radius of the circular aperture used to measure the clump fluxes.

[c] Properties based on the fluxes measured in the circular aperture of radius $r_{\rm phot}$, without subtraction of the local background from the galaxy and without aperture correction. The 1σ measurements uncertainties are computed from the noise properties of the images. The uncertainties for the ages account for those of the Hα equivalent width measurements, propagated based on the CSF model curves.

[d] Properties based on the fluxes measured in the circular aperture of radius $r_{\rm phot}$ with local background subtraction and aperture correction. For $r_{\rm phot} = 0\farcs15$, $0\farcs175$, $0\farcs20$, and $0\farcs275$, the aperture correction is a factor of 1.92, 1.68, 1.53, and 1.28, respectively. The 1σ photometric uncertainties reflect the noise properties of the images and account for both the measurement of clump and background fluxes; 3σ limits are given for clumps with background-subtracted fluxes in one or the other map that are smaller than the 3σ photometric uncertainty. The uncertainties for the ages are obtained in the same way as those based on the raw photometry.

density was approximated from the g-band luminosity synthesized from the model spectra. The effects of stellar photospheric absorption on our Hα flux measurements are negligible, and so were not accounted for in the model predictions. The variations of $W^{\rm rest}$(Hα) with stellar age depend on the SFH. The lines of constant $W^{\rm rest}$(Hα) plotted in Figure 7 are labeled with the corresponding ages for a CSF model. As an example of alternative SFHs, for exponentially declining SFRs with e-folding timescales τ, the model curves for the same ages in Figure 7 shift downward along the vertical axis and become more widely separated for ages $\gtrsim \tau$.

For CSF, the $W^{\rm rest}$(Hα) measurements imply a median stellar age of 55 Myr for the clumps and 140 Myr for the interclump pixels. For the large, luminous, and massive NIC2 clump 1, its $W^{\rm rest}$(Hα) also implies an age of 55 Myr, and so it does not appear to stand out in its evolutionary stage compared to most other clumps. The smaller, low-mass NIC2 clump 4 with lowest $W^{\rm rest}$(Hα) is the oldest clump in BX 482, with inferred age of ∼240–570 Myr depending on the treatment of the background galaxy light. The impact of various SFHs, with SFR declining or increasing with time, on the derived ages of the clumps and interclump regions is illustrated in the Appendix. In all cases, however, the relative ages are qualitatively unchanged as long as the different regions have similar SFHs. It is conceivable that the duration of the star formation activity is shorter for the localized kpc-sized clumps compared to the bulk of the stellar population across the galaxy. If so, most clumps would still be younger than the interclump regions unless they follow exponentially increasing SFHs with timescales $\tau \lesssim 50$ Myr (see the Appendix).

We can verify indirectly the validity of our hypothesis in Section 3.1 of constant observed M/L for BX 482, on the basis of the relative ages and assuming that extinction plays no role (i.e., that the relative dust obscuration is always the same across the galaxy and between the clumps). Using the same Bruzual & Charlot (2003) models, and for a given SFH, the ages inferred for the clumps and the interclump regions imply comparable M/L ratios: the scatter among clumps is $\lesssim$0.3 dex, and the median $\log(M_\star/L_g^{\rm rest})$ values of the clumps are all within ≈0.2 dex of each other for different SFHs. These results for BX 482 provide another example where the M/L of the clumps appears to be roughly constant and comparable to the ratio across the entire galaxy, as we inferred from the analysis of the $i_{814} - H_{160}$ colors for MD 41. Obviously, this conclusion should not be generalized to all galaxies, but it supports the plausibility of such an assumption in the absence of better empirical constraints.

The analysis of the extinction-insensitive Hα equivalent widths in BX 482 presented in this section revealed significant variations in the relative stellar ages among the clumps. If similar SFHs are applicable, the data provide indications that all clumps have stellar populations of comparable or younger ages than the interclump regions, with the exception of one NIC2-identified clump without Hα counterpart. In addition, there is no evidence for variations by more than a factor of a few in observed M/L ratios between clumps and interclump regions. The main uncertainty is in the SFH appropriate for different regions in BX 482, which cannot be constrained with the data currently available. In future studies, detailed spatially resolved constraints on the SFHs across galaxies will help in this respect. More accurate knowledge of absolute ages will also be important to constrain clump lifetimes, a crucial issue in the context of clump-driven scenarios for the evolution of turbulent, gas-rich disks at high redshift (see the discussion by Genzel et al. 2011, and references therein).

5. DISCUSSION

Our actively star-forming, rest-UV-selected NIC2 targets exhibit clumps in their rest-frame optical emission, just as clumps are observed in the rest-frame UV emission of many

$z \gtrsim 1$ star-forming galaxies. In the previous sections, we measured the clump properties and carefully assessed the systematic uncertainties associated with their extraction, in particular those related to the treatment of the host galaxy's background light. In this section, we now compare the properties of clumps in our NIC2 sample with those identified in other galaxy samples and at other wavelengths. We further explore constraints provided by our results on the origin of clumps and their role in the evolution of the host galaxies.

5.1. Ensemble Properties of Clumps and their Origin

5.1.1. Comparison to Clumps in Other High-redshift Galaxy Samples

The properties derived in Section 3 for the clumps in our SINS NIC2 targets agree well with the ranges for clumps in high-redshift galaxies derived from high-resolution observations at other wavelengths. The rest-frame optical sizes of ∼1 kpc of our NIC2-identified clumps are comparable to those measured in the rest-frame UV and Hα line emission of clumps identified in *HST*/ACS optical imaging and in AO-assisted SINFONI observations of $z \sim 1$–3 galaxies (e.g., Elmegreen & Elmegreen 2005; Elmegreen et al. 2009a; Genzel et al. 2008, 2011). The fractional contributions to the observed H_{160}-band emission in our SINS NIC2 objects, as well as to the observed i_{814}-band emission in MD 41 and Hα light in BX 482, are typically a few percent per clump (though with a wide range of ∼0.5%–16%), and together make up ∼10%–25% in each galaxy. These fractions are also very similar to the fractions in ACS i_{775}-band emission of rest-UV clumps in "clump-clusters" and "chains," for which Elmegreen & Elmegreen (2005) and Elmegreen et al. (2009a) derive typically ∼2% per clump and a total of ∼25% on average (ranging from $\lesssim$1% up to ∼50%) for all clumps in a given galaxy. Clump-clusters and chains are the most prominently clumpy systems in optical imaging of high-redshift galaxies in the classification of Elmegreen et al. (2004a); rest-frame UV clumps in more regular galaxies at similar redshifts tend to have lower fractional contributions (Elmegreen et al. 2009a). In Hα emission, Genzel et al. (2011) determined comparable fractions in the range <1% up to 25% for clumps in four $z \sim 2$ disks. Thus, even if the clumps are a qualitatively prominent feature of the morphologies, the apparently smoother and more extended emission component generally dominates the total galaxy light.

In terms of stellar masses, Elmegreen & Elmegreen (2005) and Elmegreen et al. (2009a) found that clumps in clump-clusters and chains appear to span a roughly constant range at $z \gtrsim 0.5$ of $M_\star^{\rm cl} \sim 10^6$–$5 \times 10^9\ M_\odot$. The clump stellar masses in our SINS NIC2 sample tend to lie in the top half of the mass distributions of Elmegreen et al. (2009a). This may reflect higher host stellar masses for most of our SINS NIC2 targets compared with the galaxies studied by Elmegreen et al. (see also the discussion by Genzel et al. 2008). It may also possibly result from our clump selection in the rest-frame optical instead of rest-frame UV as suggested by the analysis in Section 4.1 of MD 41, where NIC2-identified clumps are overall more massive than ACS-identified clumps. Obviously, the important uncertainties involved in estimating the clump properties, and the differences in methodology—notably in the treatment of the background light, and in the specifics of the modeling used to estimate masses (see Elmegreen et al. 2009a for details)—mean that only order-of-magnitude comparisons can be made between the different clump samples. Nevertheless, these various studies indicate that individual giant clumps typically each represent a few percent of the total stellar mass of the host galaxies.

In the strongly lensed $z \sim 1.5$–3 star-forming galaxies studied by Jones et al. (2010) and Swinbank et al. (2010b; see also A. M. Swinbank et al. 2011, in preparation), the sizes and dynamical masses of clumps identified in Hα or in submillimeter dust continuum and CO line emission tend to be lower (by factors of ∼2–10) than for the clumps in our SINS NIC2 objects. Aided by linear magnification factors of ∼2–35, the observations for these lensed sources reach a source-plane spatial resolution down to ≈100 pc in the best cases, undoubtedly helping to resolve smaller clumps. However, the lensed galaxies are also on average roughly twice smaller and an order of magnitude less massive than the SINS NIC2 galaxies, and have lower inferred v_c/σ_0 ratios (implying dynamically hotter disks). The differences in clump properties between the SINS NIC2 and the lensed samples may thus be more fundamentally related to the differences in host galaxy properties, as expected in the theoretical framework of gas-rich Toomre-unstable disks discussed next.

5.1.2. Comparison to Theoretical Expectations for Fragmenting Gas-rich, Turbulent Disks

Theoretical arguments as well as numerical simulations of turbulent gas-rich Toomre-unstable disks indicate that they can fragment into large and massive star-forming clumps (e.g., Noguchi 1999; Immeli et al. 2004a, 2004b; Bournaud et al. 2007; Genzel et al. 2008; Dekel et al. 2009; Agertz et al. 2009; Ceverino et al. 2010; Aumer et al. 2010; Genel et al. 2010). All our disks have high inferred local intrinsic gas velocity dispersions (∼40–90 km s^{-1}; Genzel et al. 2008; Cresci et al. 2009) and appear to be very gas-rich (gas-to-baryonic mass fractions of ∼30%–70%; Erb et al. 2006; Förster Schreiber et al. 2009; Tacconi et al. 2010). Given these global properties, a possible interpretation of the clumps seen in our five disks is that they are the result of disk instabilities. Based on high S/N AO-assisted SINFONI observations, Genzel et al. (2011) argued that giant clumps seen in Hα and in rest-UV or optical broadband emission of several large $z \sim 2$ star-forming disks (including BX 482) generally correspond to highly unstable regions in the galaxies. Indeed, Genzel et al. (2011) estimated from the AO data Toomre Q parameter values that are well below unity at the clump locations. Moreover, Genzel et al. also inferred Q values in the interclump regions below unity, suggesting global perturbations across the host disks. These findings thus appear to be consistent with the hypothesis that the observed clumps formed in situ from gravitational instabilities in gas-rich disks.

In this framework, the characteristic size and mass of the forming clumps correspond to those of the fastest growing Jeans-unstable fragmentation mode not stabilized by rotation, the Toomre scale length, and mass. These characteristic scales are related to global properties of the host galaxy and can be expressed as a function of disk radius and mass, circular velocity v_d, and local intrinsic gas velocity dispersion σ_0 (e.g., Genzel et al. 2008, 2011; Escala & Larson 2008; Elmegreen 2009; Dekel et al. 2009). The ratio of v_d/σ_0 is itself directly related to the disk scale length and scale height and is inversely proportional to the gas mass fraction. Applying Equation (5) of Genzel et al. (2011) with $Q \approx 1$ and the assumption of constant rotation velocity, the global galaxy parameters for the five disks among our NIC2 sample (from Genzel et al. 2008; Cresci et al. 2009) imply a typical Toomre radius of ∼1 kpc and mass of $\sim 4 \times 10^9\ M_\odot$. Comparable values were obtained by Genzel et al. (2008) for a

sample of eight galaxies drawn from the SINS survey, with four objects in common with our NIC2 sample (MD 41, BX 389, BX 610, and BX 482). For $Q < 1$, these size and mass estimates would increase (all other galaxy parameters being fixed).

The Toomre length and mass inferred above are of the same order as the intrinsic sizes and stellar masses for the resolved clumps in the disks of our NIC2 sample. The total masses could be significantly larger than the stellar masses if the clumps were themselves very gas-rich. Assuming that the typical gas-to-baryonic mass fraction of ∼50% for the SINS NIC2 disks is representative for the clumps, the inferred total mass for the resolved disk clumps would be in even closer agreement with the expectations. Direct molecular gas mass measurements for individual clumps in our targets are not yet available. However, estimates can be made for BX 482 with AO-assisted SINFONI data from Hα-based SFRs and using the "Kennicutt–Schmidt" relation. Following Genzel et al. (2011), to which we refer for details of the calculation and the choice of Kennicutt–Schmidt relation (slope and zero point) that might be most appropriate on the 1 kpc-scales of clumps in high-redshift star-forming disks, the "background-subtracted" Hα measurements imply $M_{\rm gas}^{\rm cl}$ from $<6 \times 10^8\,M_\odot$ for clump 2 to $\sim 5 \times 10^9\,M_\odot$ for clump 1 (see also Genzel et al. 2011, their clump "BX482-A"), with a median of $\sim 10^9\,M_\odot$ (including limits). These estimates include a 36% correction for helium and metals, account for the Chabrier (2003) IMF adopted in this paper, and assume that the global $A_V = 0.8$ mag from the SED modeling of BX 482 is representative of the extinction toward the clumps. The gas mass for clump 1, the brightest among our NIC2 sample, is comparable to those derived by Genzel et al. (2011) for other bright clumps in three additional $z \sim 2$ disks. For the NIC2-identified clumps in BX 482, our results give $M_{\rm gas}^{\rm cl}$ roughly twice the $M_\star^{\rm cl}$ estimates, and the total (stellar + gas) clump masses with median $\sim 1.5 \times 10^9\,M_\odot$. The implied gas-to-baryonic mass fractions of ∼60%–70% for the clumps are comparable to the galaxy-integrated value (Förster Schreiber et al. 2009).

The theoretical expectations computed here as well as the empirical measurements should be regarded as rough estimates in view of the simplifying assumptions and the large uncertainties associated with the determination of clump properties. In addition, differences between expectations and measurements can plausibly arise from different global galaxy properties at the time when the observed stellar clumps were formed and from evolution in clump properties (e.g., through mass loss). Notwithstanding these limitations, the agreement between the predictions and the observed properties is remarkable and provides a framework to interpret the prominent clumpy features in distant galaxies. Similar conclusions were reached by Jones et al. (2010) for the origin of clumps in their lensed galaxy sample, based on the measured clump sizes and the expectations computed with the size, mass, and dynamical properties of the host disks. As pointed out in previous studies (Escala & Larson 2008; Elmegreen 2009; Genzel et al. 2011, and references therein), the high gas mass fractions and low $v_{\rm d}/\sigma_0$ ratios observed in $z \gtrsim 1$ disks naturally lead to the formation of larger self-gravitating, star-forming complexes than in the less gas-rich, dynamically cold, and geometrically thin $z \sim 0$ disks. In addition, the presence of a massive stabilizing stellar disk and/or bulge in local mature disk galaxies also leads to smaller lower-mass star-forming complexes, or even to the suppression of their formation (e.g., Bournaud et al. 2007; Dekel et al. 2009; Ceverino et al. 2010).

5.2. Constraints on Radial Age Variations and Clump Evolution

In the scenario outlined in the previous section, the massive star-forming clumps are expected to migrate toward the gravitational center as a result of dynamical friction against the host disk and of clump–clump interactions. Ultimately, the clumps may coalesce into a young bulge within ∼10 dynamical timescales (Noguchi 1999; Immeli et al. 2004a, 2004b; Bournaud et al. 2007; Genzel et al. 2008; Dekel et al. 2009; Agertz et al. 2009; Ceverino et al. 2010) unless they are rapidly disrupted, for instance by stellar feedback or tidal torques. In that respect, recent theoretical work has highlighted the possibly dramatic impact on clump evolution of vigorous star formation feedback (Murray et al. 2010; Genel et al. 2010; but see Krumholz & Dekel 2010 for a contrasting view). High-resolution and high S/N SINFONI observations have provided the first empirical evidence of gas outflows originating from massive luminous clumps in $z \sim 2$ disks (Genzel et al. 2011). In some of the most actively star-forming clumps, the outflow could be sufficiently strong to disperse a large fraction of the initial gas before they reach the center of the galaxies. If the clumps do survive long enough and spiral inward, they are then expected to exhibit a significant age spread, with older clumps typically closer to the center of the galaxy (e.g., Elmegreen et al. 2009a; Krumholz & Dekel 2010).

Our results for BX 482 seem broadly consistent with this picture. From measurements of the age-sensitive Hα equivalent width, we found in Section 4.2 indications of age variations among the NIC2- and Hα-identified clumps. Figure 8 shows the distribution of $W^{\rm rest}$(Hα) and of the corresponding stellar ages assuming CSF as a function of deprojected galactocentric distance d. Although the data do not reveal a significant correlation between $W^{\rm rest}$(Hα) or age and d (a Spearman's rank correlation analysis yields a coefficient of about 0.65 but with a significance of $\approx 1.5\sigma$), there is a clear distinction driven by the NIC2-identified clump 4 already highlighted in Section 4.2.[21] This clump, with the lowest Hα equivalent width and oldest age, is also nearest the center of BX 482 at $d = 2.9$ kpc. The six other clumps, with higher equivalent widths and younger ages, are located at significantly larger $d \approx 5$–7.5 kpc. This distinction is qualitatively preserved for alternative choices of SFH as long as the clumps follow similar SFHs (see the Appendix).

For MD 41, the stellar ages cannot be constrained directly but the deprojected radial distribution of $i_{814} - H_{160}$ colors of the clumps can provide indications of maturity in terms of M/L ratio. The colors are plotted as a function of galactocentric distance d in Figure 9, along with the derived $M_\star/L_g^{\rm rest}$ ratios. These plots suggest a weak trend (with Spearman's rank correlation coefficient of ≈0.85 and significance of 2σ) of redder colors and higher M/L ratios at smaller radii; it is mostly dominated by clump NIC2-1 and ACS-3, which, as noted in Section 4.1.2, exhibit the most distinct colors compared with the ensemble of clumps and interclump regions.[22] If the dust extinction and the SFHs are similar among the clumps, the radial distribution of colors and M/L could be indicative of older stellar ages for clumps at smaller galactocentric distances.

[21] The distribution of $W^{\rm rest}$(Hα) with d over the interclump pixels in BX 482 shows a large scatter with hardly any trend ($\rho \approx 0.18$ at the 2σ level), reflecting the overall very similar appearance of the Hα and H_{160}-band emission discussed in Section 4.2.

[22] The distribution of $i_{814} - H_{160}$ colors with d over the interclump pixels in MD 41 is almost flat, with increasing scatter at larger radii (and $\rho \approx 0.15$ at the 2σ level), as indicated by the fairly uniform colors across MD 41 with the exception of some of the clumps as highlighted in Section 4.1.

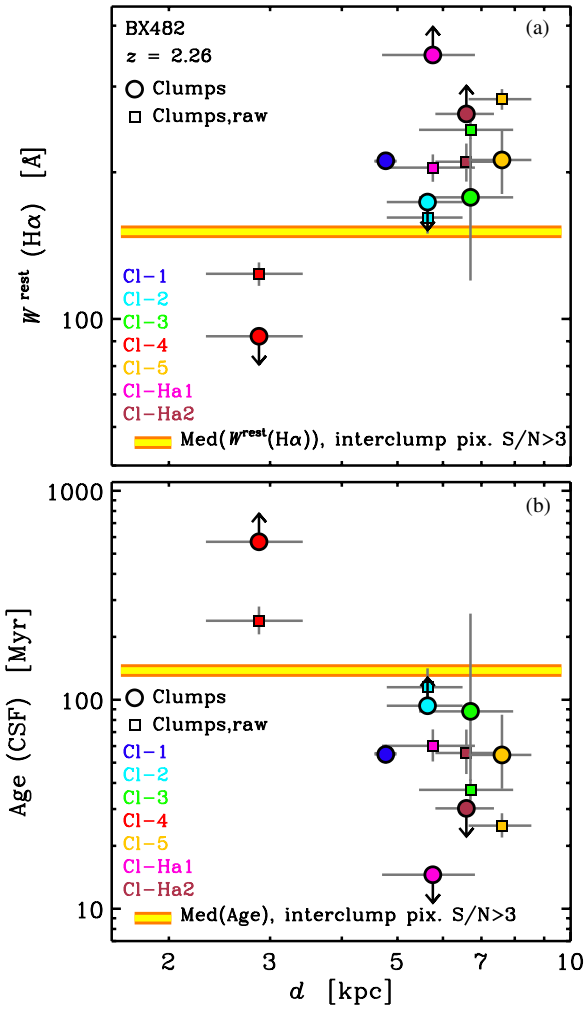

Figure 8. Properties as a function of deprojected galactocentric distance of clumps in BX 482. (a) Rest-frame Hα equivalent width, computed from the SINFONI Hα map and the NIC2 H_{160}-band image as described in Section 4.2.2. Results based on the "background-subtracted" and "raw" photometry are plotted as circles and squares, respectively. Different colors indicate different clumps, as labeled in the plot. Error bars correspond to the formal photometric uncertainties. For clumps undetected in one or the other image, 3σ upper limits on their background-subtracted photometry are used. The thick yellow–orange line shows the median $W^{\rm rest}$(Hα) measured for pixels in the interclump regions with an S/N > 3 in each map. (b) The same as panel (a) but for the stellar ages derived from comparison of the $W^{\rm rest}$(Hα) measurements to model predictions for a constant star formation rate, as described in Section 4.2.3. The uncertainties of the ages account for the photometric measurements uncertainties. The clump closest to the center of BX 482, NIC2-4, is clearly distinct from the ensemble of the other clumps farther out in radius, with its $W^{\rm rest}$(Hα) implying the oldest age of all clumps. All other clumps have comparable or higher $W^{\rm rest}$(Hα), hence younger inferred ages, than the median for the interclump regions. For different star formation histories (SFHs), the absolute ages can change significantly but the relative ages between clumps and interclump regions are qualitatively unchanged as long as the different regions have similar SFHs.

(A color version of this figure is available in the online journal.)

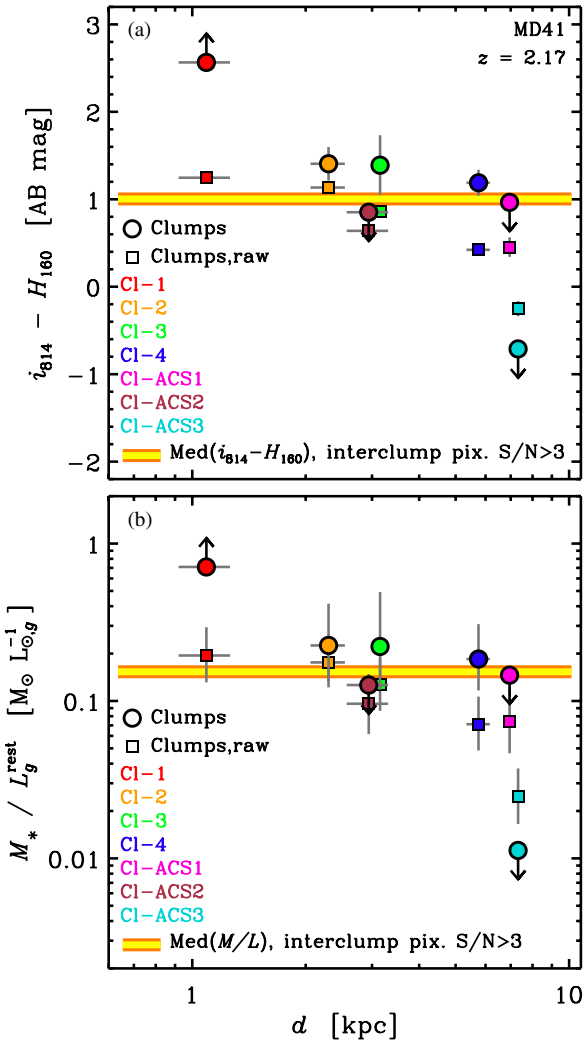

Figure 9. Properties as a function of deprojected galactocentric distance of clumps in MD 41. (a) Observed $i_{814} - H_{160}$ colors, computed from the ACS i_{814}-band and NIC2 H_{160}-band maps as described in Section 4.1.2. Results based on the "background-subtracted" and "raw" photometry are plotted as circles and squares, respectively. Different colors indicate different clumps, as labeled in the plot. Error bars correspond to the formal photometric uncertainties. For clumps undetected in one or the other band, 3σ upper limits on their background-subtracted photometry are used. The thick yellow–orange line shows the median color measured for pixels in the interclump regions with an S/N > 3 in each band. (b) The same as panel (a) but for the ratio of stellar mass to dust-attenuated rest-frame g-band luminosity derived using the relationship between observed $i_{814} - H_{160}$ colors and $M_\star/L_g^{\rm rest}$ at $z = 2.2$, as described in Section 4.2.3 (see also Paper I). The uncertainties of the M/L ratios account for those of the photometry as well as for the estimated accuracy of the color–M/L relationship. Clumps closer to the center of MD 41 tend to have redder colors, hence higher observed $M_\star/L_g^{\rm rest}$ ratios, which could reflect increasing stellar ages and/or dust extinction of clumps at smaller radii.

(A color version of this figure is available in the online journal.)

In their studies of clumpy $z \sim$ 1–4 galaxies in the H-UDF, Elmegreen & Elmegreen (2005, from ACS B_{435}-, V_{606}-, i_{775}-, and z_{850}-band imaging) and Elmegreen et al. (2009a, using the same ACS bands, complemented with NICMOS/NIC3 J_{110}- and H_{160}-band imaging) found that ACS i_{775}-band-identified rest-frame UV clumps within a given galaxy mostly span a narrow range of colors and that the interclump regions tend to be redder, which they interpreted in terms of older ages for the underlying stellar population across the host galaxy. In ~30%–50% of the H-UDF chains and clump-clusters, and in all their "spiral" types, Elmegreen et al. (2009a) also identified clumps that are prominent in the near-IR bands, exhibit redder colors, and tend to lie closer to the galaxies' centers. These "bulge-like clumps" (or bulges for spirals) have higher inferred stellar ages and masses than the other clumps present within the same galaxy; they do not appear to differentiate significantly in terms of star formation decay timescales or extinction. Moreover, these differences in stellar ages and masses are more important for spirals and less significant for clump-clusters and chains. The derived stellar ages of clumps span a wide range, centered around ~100 Myr.

As argued by Elmegreen et al. (2009a, see also Elmegreen et al. 2009b), the inferred clump ages and the presence of a redder and more massive clump generally closer to the center in clumpy and spiral types are consistent with inward clump migration, and suggest that at least a fraction of the clumps may survive long enough to reach the central few kpc.

The trends of redder colors for the clumps in MD 41 and of older ages for those in BX 482 at smaller galactocentric radii are consistent with the general findings of Elmegreen, Elmegreen, and coworkers. Our higher resolution NIC2 imaging, compared with NIC3, allowed us, however, to detect clumps directly from longer wavelengths on ∼1 kpc scales. The NIC2 data furthermore provide a better match to the ACS PSF enabling us, in the case of MD 41, to identify and measure the properties of clumps consistently in both the optical and near-IR bands. While most ACS-identified clumps in MD 41 tend to be bluer than the interclump regions, in line with the results of Elmegreen et al. (2009a), the NIC2-identified clumps have in contrast comparable or redder colors. The small but systematic differences in $i_{814} - H_{160}$ colors, and in derived M/L ratios and stellar masses, between the NIC2- and ACS-identified clumps would suggest that clumps identified in the rest-optical and rest-UV are complementary and probe together a wider range in properties. We can draw a similar conclusion for the clumps identified in rest-frame optical and Hα in BX 482, with the NIC2 and SINFONI PSFs also well matched to each other, although there is more overlap here. The clump ages in BX 482 for CSF models are compatible with the range for clumps at $z \sim 2$ by Elmegreen et al. (2009a); clump NIC2-4 closest to the center lies at the high age end, whereas all others are in the younger half of the Elmegreen et al. distribution.

The dynamical timescale $t_{\rm dyn} = r/v$ at the effective radius ≈ 6 kpc of BX 482 is ≈25 Myr (correspondingly, the orbital timescale is $t_{\rm orb}(r = R_{\rm eff}) \approx 160$ Myr). If the clumps have been forming stars at a roughly constant rate, the stellar age of the oldest clump NIC2-4 thus implies that it has survived for ∼10 to ≳20 dynamical timescales, depending on whether the raw or background-subtracted Hα equivalent width estimates is adopted. It thus appears plausible that this clump has formed at larger radii and has migrated to its present location closer to the center at $d = 2.9$ kpc. The other younger clumps have ages ∼(1–4) × $t_{\rm dyn}$, so that they may still be located fairly close to the radius at which they formed. For the largest and brightest clump NIC2-1, Genzel et al. (2011) detected a broad (FWHM ≈ 400 km s^{-1}) and somewhat blueshifted (by several 10 km s^{-1}) Hα line component, which is interpreted as a sign of outflowing gas. Combining estimates of the outflow kinematics and rate, and of the clump extent, gas mass, and gas-phase oxygen abundance, Genzel et al. (2011) derived gas dispersion, outflow expansion, and chemical enrichment timescales in the range ∼0.3–1 Gyr. These estimates would imply longer clump lifetimes than our $W^{\rm rest}$(Hα)-based stellar age for CSF of ≈55 Myr, and may suggest that this clump has survived for more than a couple dynamical timescales.

5.3. Constraints on a Stellar Bulge/Inner Disk Component

Clump migration may provide an important mechanism for growing a stellar bulge and/or inner disk component in high-redshift galaxies (e.g., Noguchi 1999; Immeli et al. 2004a, 2004b; Bournaud et al. 2007; Carollo et al. 2007; Elmegreen et al. 2009a; Ceverino et al. 2010), along with other internal mechanisms such as stellar bar-induced streaming (e.g., Bournaud & Combes 2002) or viscous drag in a gaseous disk (e.g., Lin & Pringle 1987; Silk 2001). In $z \sim 0$ disks, these secular processes occur on long timescales of at least several Gyrs (e.g., Kormendy & Kennicutt 2004). At $z \sim 2$, however, disk galaxies are significantly more gas-rich, and their gas phase appears to be much more turbulent. Under these conditions, secular processes should proceed faster by an order of magnitude or more (e.g., Noguchi 1999; Immeli et al. 2004a, 2004b; Bournaud et al. 2007; Genzel et al. 2008, 2011; Ceverino et al. 2010). If clumps are dispersed and lose mass before reaching the very center of the galaxy, the buildup of a bulge component through clump migration would be slower but this mechanism could still contribute to inward mass transfer (e.g., Bournaud et al. 2007; Elmegreen et al. 2009b).

From duty cycle arguments, Elmegreen et al. (2009a) inferred that the clumpy phase in high-redshift disks may last for several Gyrs, or 5–10 clump formation epochs. Some recent high-resolution cosmological simulations suggest that rapid accretion from the halo along narrow, cold streams replenishing the gas reservoir of high-redshift disks could help to maintain the clumpy phase over such extended timescales (Dekel et al. 2009; Ceverino et al. 2010). One may therefore expect the presence of a more important stellar bulge or inner disk component in more mature galaxies, as inward migration of previous clump generations and secular processes would have had more time to transport material in the central regions.

In this context, an immediate question is whether our data provide evidence for a more important stellar bulge or inner disk component in our NIC2 sample disks with older stellar populations. At first glance, such a trend is not apparent from the observed spatial distribution of the rest-frame optical continuum emission seen in our NIC2 H_{160}-band images. The best-fit Sérsic index n does not show any significant correlation with best-fit stellar age from the rest-UV/optical SED modeling, as discussed in Paper I. The implied stellar mass fraction of the clump closest to the center in each of the disks, if interpreted as a young bulge, also shows no trend with galaxy stellar age. More generally, none of the disks in our sample show obvious signs of a prominent centrally concentrated stellar component apart from BX 663, for which the two-component Sérsic model fits in Paper I suggest that the central peak could be associated with a fairly compact $n = 4$ bulge-like component contributing ≈35% of the total H_{160}-band luminosity. However, there could be an older stellar population in the inner parts of the galaxies eluding detection even at rest frame ≈5000 Å if it has a significantly higher M/L ratio than the stellar population dominating the observed rest-frame UV to optical SED.

To set constraints on the mass contribution of such a hidden stellar component, we postulated that this component has an effective radius $R_{\rm e} = 1$ kpc and Sérsic index $n = 3$ akin to the compact quiescent $z \sim 2$ K-selected galaxies of van Dokkum et al. (2008; see also Kriek et al. 2009), and assumed a fixed axis ratio $b/a = 1$. In what follows, we refer to this component as "bulge," motivated by our choice of structural parameters, but we note that other interpretations are not excluded. We estimated how much extra light from this component is allowed by the 1σ uncertainties of the observed radial light profiles at $r < 2$ kpc for each of the five disks among our NIC2 sample, as illustrated in Figure 10. To determine the corresponding stellar mass contributions, we considered in turn different $M_\star/L_g^{\rm rest}$ ratios. Arguably, a realistic choice is the typical M/L found for $z \sim 2$ compact quiescent galaxies (see Kriek et al. 2009). For the van Dokkum et al. (2008) sample, the median $M_\star/L_g^{\rm rest}$ [$M_\odot\, L_{g,\odot}^{-1}$] ≈ 0.6 based on the SED modeling of

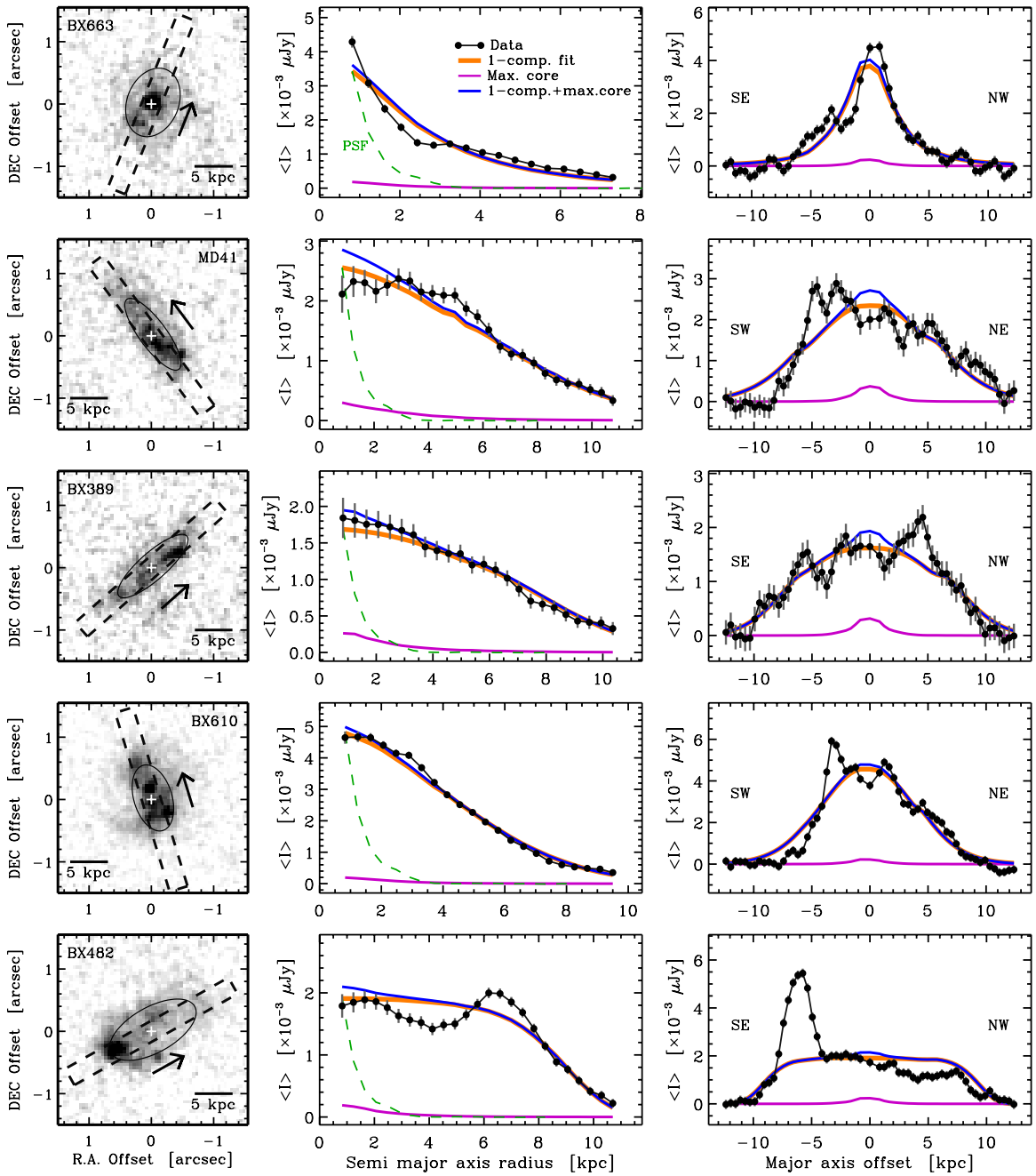

Figure 10. Images and light profiles extracted from the NIC2 images of the five disks among our SINS NIC2 sample. Each row corresponds to one galaxy, and the panels are as follows. Left: H_{160}-band maps on a linear gray-scale intensity scale. An ellipse is drawn, centered at the geometric center of each galaxy, with semimajor axis length, axis ratio, and P.A. corresponding to the best-fit parameters of the single-component Sérsic model fits of Paper I. The rectangle shows the pseudo-slit used to extract the major axis light profiles. North is up, east is to the left. Middle: radial light profiles extracted in annuli of increasing radius, with center, axis ratio, and P.A. given by the best-fit single-component Sérsic model ("disk") to the H_{160}-band two-dimensional surface brightness distribution of each galaxy. The profiles are shown for the data (black solid line and filled dots), the best-fit "disk" component (thick orange line), the "maximal" bulge component with $R_e = 1$ kpc, $n = 3$, and $b/a = 1$ allowed by the 1σ measurements uncertainties at $r < 2$ kpc (magenta solid line; see Section 5.3), and the sum of the "disk" and "maximum bulge" (blue solid line). The circularly symmetric light profile of the PSF is plotted for reference (green dashed line). Right: major axis light H_{160}-band light profiles extracted along the pseudo-slit of width 0.″3 shown in the left panels; negative (positive) offsets relative to the center correspond to the south (north) side of the galaxy. Different colors for the lines are the same as for the middle panels.

(A color version of this figure is available in the online journal.)

Kriek et al. (2008), after adjustment to the Chabrier (2003) IMF adopted in this work.[23] This value is uncorrected for dust extinction, but the median A_V for the quiescent sample is similar to that of our five SINS NIC2 disks (0.7 mag versus 0.8 mag, respectively). This "passive" M/L is, however, comparable to or lower than the ratio for our three disks with oldest stellar ages. If there was an important bulge characterized by such an M/L ratio, it would be clearly seen in the data. We therefore explored the more extreme scenarios in which all stars of the hidden bulge are as old as the age of the universe at the redshift of each disk,

[23] The difference between $M_\star/L_g^{\rm rest}$ relevant for our data and $M_\star/L_V^{\rm rest}$ given by Kriek et al. (2008) is <10% for the typical ages, A_V, and SFHs of the quiescent galaxies.

Table 5
Estimates of the Contribution of a Central Stellar Bulge Component in the SINS NIC2 Sample Disks

Property[a]	Case[b]	BX 663	MD 41	BX 389	BX 610	BX 482
$\mathcal{F}^{\rm bulge}(H_{160})$	...	0.017	0.035	0.034	0.012	0.013
$\mathcal{F}^{\rm bulge}(M_\star)$	Passive M/L	$0.018^{+0.000}_{-0.001}$	$0.26^{+0.01}_{-0.02}$	0.026 ± 0.000	0.011 ± 0.000	0.050 ± 0.001
$\mathcal{F}^{\rm bulge}(M_\star)$	Max. old SSP, $A_V = 0$ mag	0.039 ± 0.001	$0.64^{+0.03}_{-0.04}$	0.063 ± 0.000	0.026 ± 0.001	0.12 ± 0.00
$\mathcal{F}^{\rm bulge}(M_\star)$	Max. old SSP, $A_V = A_{V,\rm SED}$	$0.092^{+0.002}_{-0.003}$	$2.34^{+0.10}_{-0.14}$	0.19 ± 0.00	$0.063^{+0.001}_{-0.003}$	$0.28^{+0.00}_{-0.01}$

Notes.
[a] $\mathcal{F}^{\rm bulge}(H_{160})$ is the estimated maximum contribution to the total H_{160}-band emission of each galaxy of a putative hidden bulge component with effective radius $R_{\rm e} = 1$ kpc and Sérsic index $n = 3$ (see Section 5.3). $\mathcal{F}^{\rm bulge}(M_\star)$ is the corresponding fraction of the total galaxy stellar mass derived from the rest-UV/optical SED modeling. Uncertainties on the latter reflect the ranges of fractional contributions when varying the hidden bulge $R_{\rm e}$ up to 3 kpc, and n between 2 and 4. The range for the fraction of light for $n = 2$ and 4 are within <0.5% at the values for $n = 3$ for all galaxies.
[b] Different assumptions were made on the M/L ratio of the hidden bulge: a ratio corresponding to the median value of the massive quiescent $z \sim 2$ galaxy sample of van Dokkum et al. (2008), and that of a maximally old SSP whose light is unobscured or attenuated by the same amount as inferred from the SED modeling of each galaxy (see Section 5.3).

and whose light is either unobscured or attenuated by the same amount as the stars that dominate the rest-UV/optical SED. The M/L for this maximally old single stellar population (SSP) is calculated from the same Bruzual & Charlot (2003) models for solar metallicity as used in Paper I for the SED fitting.

The results are reported in Table 5. The light contribution $\mathcal{F}^{\rm bulge}(H_{160})$ corresponds to the fraction of the total observed H_{160}-band flux density for each galaxy, and the mass fraction is relative to the stellar mass obtained from the SED modeling, $\mathcal{F}^{\rm bulge}(M_\star) \equiv M_\star^{\rm bulge}/M_\star^{\rm SED}$. The uncertainties given in Table 5 reflect the (small) impact of varying the bulge Sérsic index between $n = 2$ and 4, and of increasing the $R_{\rm e}$ up to 3 kpc. Unsurprisingly, the light fractions are very small, in the range 1%–3.5%. In terms of stellar mass, the highest fractions hidden in an older bulge are found for the disks with youngest ages (hence lowest $M_\star/L_g^{\rm rest}$ ratios) from the best-fit SED model. Nevertheless, the mass fractions are small to moderate only, ranging from a few percent to ≈30%, with the exception of MD 41 (with estimates of up to a factor of ∼2.3, but see below). For all objects, the sum of $M_\star^{\rm SED} + M_\star^{\rm bulge}$ does not exceed the total dynamical mass (Genzel et al. 2008; Cresci et al. 2009), even when accounting for the substantial amounts of gas inferred (Förster Schreiber et al. 2009; Tacconi et al. 2010). A further plausibility check for our assumptions can be made for MD 41 by comparing the resulting M/L ratio for the various cases with the $i_{814} - H_{160}$ color-based estimates in the inner $r \lesssim 1$ kpc. Only the maximally old obscured bulge scenario leads to an $M_\star/L_g^{\rm rest}$ value that is largely different from the ratio corresponding to the observed colors, suggesting that this case (with more than twice the stellar mass being hidden) may be regarded as unlikely. More generally, the maximally old SSP assumption is an extreme one and the results should be considered as upper limits.

We conclude from the exercise above that the disks in our NIC2 sample are unlikely to contain an important fraction of their stellar mass in an old bulge or inner disk unseen in our H_{160}-band data, with the possible exception of MD 41. BX 663 appears to be the only object in which a significant bulge-like component is directly visible, if the AGN contribution to the rest-frame ≈5000 Å emission can be neglected. The visible and hidden mass estimates add up to $\sim 1 \times 10^9$ to $3 \times 10^{10}\ M_\odot$ in the central $r \lesssim 1$ kpc regions of our SINS NIC2 disks; thus, it appears that none of these disks host a compact massive core. No trend between stellar population age and the importance of a central stellar component emerges when accounting for an old hidden population.

Interestingly, Genzel et al. (2008) found in contrast evidence for a connection between central dynamical mass concentration and maturity of the stellar population, with the ratio of dynamical mass enclosed within $r \approx 3$ and 10 kpc increasing with older stellar age and higher inferred metallicity of the galaxies. For the four objects in common with our NIC2 sample, Genzel et al. derived $M_{\rm dyn}(r < 3\,{\rm kpc})/M_{\rm dyn}(r < 10\,{\rm kpc}) < 0.15$ for MD 41, 0.21 for BX 482, and 0.39 for both BX 389 and BX 610. Combining the observed H_{160}-band light profiles from our NIC2 data together with the constraints on the mass of a hidden evolved bulge, we find that the implied stellar mass concentration calculated in the same manner agrees reasonably well with the value inferred from the dynamics for BX 482 and BX 610. On the other hand, there are significant differences between the central stellar and dynamical mass concentrations for MD 41 and BX 389.

Thus, despite our findings in Section 4 consistent with inward clump migration—a possible mechanism for growing stellar bulges or inner disks over time—our SINS NIC2 disks do not appear to show a trend of higher central stellar mass concentration with older galaxy age even when accounting for a possible hidden component. Admittedly, our sample may be too small and may sample too sparsely different evolutionary stages between the objects with younger (∼50–320 Myr) and older (∼2.5–2.8 Gyr) stellar ages, to discern such a trend. Moreover, various factors could obviously complicate the analysis presented in this section, including the unknown spatial variations in extinction and in the distribution of the gas, which contributes a large fraction of the total mass in these galaxies. Detailed maps constraining the extinction and gas mass distribution, in addition to the M/L ratio and the kinematics, will be important to further test the scenario of bulge/inner disk growth through clump migration and secular processes.

5.4. Other Interpretations of the Clumpy Features

In this paper, we assumed that the compact regions of higher apparent rest-frame optical surface brightness across our SINS NIC2 targets represent genuine substructure in the distribution of the stellar populations. As we discussed earlier in this section, the properties derived for these clumps as well as the global properties of the host galaxies are consistent with the scenario in which giant massive clumps result from gravitational instabilities in gas-rich, turbulent disks. This scenario provides a framework to interpret clumpy morphologies and to investigate dynamical processes that may play an important role in the buildup of bulges and inner disks in high-redshift galaxies.

Other interpretations are possible. Bright clumps could represent merger components. BX 528 is a case where at least two of the clumps identified most likely correspond to the progenitor galaxies of a major merging pair, and the southern clump 4 in BX 389 is plausibly a small companion galaxy (Paper I). Clumps within disk galaxies could also be of external origin, and correspond to newly accreted low-mass systems. The distinction between clumps formed in situ and those accreted from the halo is not easy. Constraints could be obtained from an accurate analysis of the stellar properties of clumps and host galaxies including age and metallicity, or from a detailed baryonic and dynamical mass budget of clumps to test whether they contain dark matter. Arguably, it may seem however rather unlikely that as many as 5–10 clumps per galaxy all originate from rapid accretion of satellites or clumps brought in from the halo along filaments or dense, cold narrow streams (e.g., Elmegreen et al. 2008; Dekel et al. 2009; Agertz et al. 2009; Ceverino et al. 2010).

Another possibility is that the kpc-sized clumps simply correspond to locations across galaxies with lower line-of-sight dust obscuration. Here again, the distinction between real substructure in the stellar populations or star-forming regions and regions of lower obscuration would necessitate detailed spectral or multi-wavelength constraints on resolved scales of 1 kpc or smaller to pin down accurately the variations in extinction across the galaxies. The role of extinction in clumpy morphologies is certainly a more important concern in studies based on rest-frame UV imaging compared with rest-frame optical imaging, but it could still play a significant role at rest frame ≈5000 Å, as is well known from nearby dusty star-forming galaxies. Small fractions of light of a few percent, as inferred for most clumps in our SINS NIC2 sample as well as on average for clumps in optical imaging of high-redshift galaxies, do not rule out this interpretation, although it appears less plausible in the case of very bright clumps with fractions in excess of ∼10%. Extinction effects may also naturally explain the findings by Elmegreen et al. (2009a) that rest-UV-identified clumps tend to have bluer colors than the interclump regions. It may be more difficult to reconcile with the trend of redder colors we found for rest-optically identified clumps in MD 41, or the "bulge-like" clumps often at more central locations in galaxies discussed by Elmegreen et al. (2009a). If large localized spatial variations in extinction are responsible for the clumpy features in our galaxies, trends of redder colors and older ages at smaller radii, as inferred for MD 41 and BX 482 in Section 4.2, could reflect age gradients in the underlying stellar population, dominated by younger stars at larger radii and older ones in a bulge or inner disk component.

Possibly, clumpy features in high-redshift galaxies have multiple causes. In future studies, high spatial resolution multi-wavelength mapping and sensitive spectroscopy will be essential to determine robustly the nature of clumps. More realistically in the near future, a combination of optical and near-IR imaging (allowing spatially resolved SED modeling), AO-assisted integral field spectroscopy (mapping the kinematics and star formation, and providing additional constraints on the age and SFH), and millimeter interferometry (mapping directly the molecular gas distribution and kinematics) will allow tighter constraints on the detailed physical, stellar, and dynamical properties of clumps. The first steps taken in this direction (e.g., Elmegreen & Elmegreen 2005; Elmegreen et al. 2009b; Genzel et al. 2011; Tacconi et al. 2010; Jones et al. 2010; Swinbank et al. 2010b; A. M. Swinbank et al. 2011, in preparation) show that, while challenging, such an approach will provide key information necessary to better understand the nature of the observed kpc-scale substructure and its role in the evolution of distant galaxies.

6. SUMMARY

We have studied the characteristics of the clumpy features based on *HST*/NIC2 H_{160}-band imaging for a unique sample of six $z \sim 2$ star-forming galaxies with VLT/SINFONI integral field spectroscopy. The NIC2 imaging provides good sampling of the *HST* PSF at 1.6 μm and allows us to reliably detect substructure in the rest-frame optical emission on scales as small as 1.2 kpc at the $z = 2.1$–2.5 of our targets. We have identified "clumps" through a systematic detection procedure that takes into account both host galaxy background subtraction and PSF deconvolution for estimating the clump luminosities, stellar masses, and sizes. We assessed for the first time in detail the systematic uncertainties associated with extracting clump properties in distant galaxies, especially in terms of the treatment of the underlying host galaxy light. We interpreted the properties of the clumps in the framework of gas-rich, turbulent disks in which giant massive clumps can form through violent gravitational instabilities. Our study complements previous work focusing on clumps identified in the rest-frame UV or in Hα line emission, and shows the importance of including constraints at longer wavelengths and on the same ∼1 kpc scales for a more complete picture.

Our main results can be summarized as follows.

1. We identified between two and seven clumps per galaxy in their rest-frame optical emission. Using the SINFONI data, we determined that these clumps are unlikely to be caused predominantly by strong nebular emission lines within the H_{160} bandpass and thus must reflect compact sources of stellar continuum light. At least two of the clumps in the kinematically identified binary merger BX 528 are likely associated with the merging galaxies. For the large kinematically confirmed disk BX 389, the clump most offset from the main body of the galaxy can be securely identified as a small nearby companion at a projected distance of ≈5 kpc. Continuum light from a stellar bulge component could plausibly dominate the central prominent peak in BX 663. In terms of size, luminosity, and stellar mass, these specific clumpy features do not differentiate significantly from the ensemble of all clumps identified in our NIC2 targets, emphasizing the importance of taking into account the nature of the host system from the dynamics, morphologies, and spectral properties in the interpretation of "clumps." All other clumps may have plausibly formed in situ from fragmentation of the turbulent, gas-rich disks of our targets.
2. The stellar clumps in the H_{160}-band images of our NIC2 targets generally represent surface brightness enhancements of ∼25%–35% relative to the surrounding background from the host galaxy. This contrast is substantially lower than for clumps identified in optical ACS imaging of $z \sim 1$–4 prominently clumpy galaxies (clump-clusters and chains), which generally appear to be brighter than the background by factors of ∼2–4 (e.g., Elmegreen et al. 2009a). The contribution of individual clumps to the total galaxy H_{160}-band emission is of a few percent typically, although with wide range from the faintest (≈0.5%) to the brightest (≈16%). The total contribution of all clumps in a given galaxy is between 10% and 25%. The typical intrinsic rest-frame

optical FWHM size of our clumps is ∼1 kpc, similar to sizes of clumps identified and measured in the rest-UV continuum and Hα line emission (e.g., Elmegreen & Elmegreen 2005; Elmegreen et al. 2009a; Genzel et al. 2008, 2011). The inferred stellar masses have a median $\sim 10^9\ M_\odot$, and a range that lies within the more massive half of the distribution inferred for rest-UV-identified clumps (Elmegreen & Elmegreen 2005; Elmegreen et al. 2009a), possibly reflecting the higher stellar masses of our galaxies and the clump identification at longer wavelengths.

3. By combining the NIC2 data with *HST* ACS i_{814}-band imaging available for MD 41, and existing AO-assisted SINFONI Hα data for BX 482, we inferred modest color, M/L, and stellar age variations among most clumps within each galaxy, and between clumps and interclump regions. In these two objects, the sets of clumps identified at different wavelengths do not fully overlap. In MD 41, NIC2-identified clumps tend to have redder $i_{814} - H_{160}$ colors than ACS-identified clumps and than the interclump regions. The colors for the reddest and bluest clumps appear to require differences in stellar age in addition to extinction effects. In BX 482, we derived more robust constraints on the relative stellar ages from the Hα equivalent width, taken as the Hα line to rest-frame ≈5000 Å continuum ratio. Assuming similar SFHs, the NIC2-identified clumps tend to be older than the Hα-identified clumps but, except for one, have ages younger than the interclump regions. These findings suggest that clumps identified at different wavelengths are complementary and probe together a wider range in clump properties. Most importantly, clumps in MD 41 and BX 482 that are closer to the center appear to show more maturity in terms of stellar populations.
4. The quantitative constraints on clump properties for the kinematically confirmed disks in our SINS NIC2 sample are consistent with the scenario in which giant massive clumps form from disk instabilities. Their sizes and masses are of the order of the Toomre scale length and mass expected for disks with the same global properties as measured for the galaxies (large gas velocity dispersion, high gas mass fractions, and disk sizes). The trends of older and/or more obscured stellar populations of clumps at smaller galactocentric radii for BX 482 and MD 41 are consistent with inward migration of the massive clumps through dynamical friction and clump–clump interactions. These findings suggest that a fraction of the clumps can survive destruction by stellar feedback or other disruptive mechanisms for at least a few dynamical timescales. Our results add to other evidence from previous studies of high-redshift clumpy galaxies (e.g., Genzel et al. 2008; Elmegreen et al. 2009a) and from numerical simulations of gas-rich unstable disks (e.g., Noguchi 1999; Immeli et al. 2004a, 2004b; Bournaud et al. 2007; Agertz et al. 2009; Ceverino et al. 2010) that clump migration could be an important mechanism by which material is transported in the inner regions of young disk galaxies, contributing to the buildup of a bulge and inner disk component.
5. We estimated for the disks in our sample $\sim 1 \times 10^9$ to $3 \times 10^{10}\ M_\odot$ in a stellar bulge or inner disk component at $r \lesssim 1$–3 kpc, with no obvious trend emerging among these five sources between central stellar mass fraction and stellar age of the galaxy. Our galaxies appear to have roughly at least an order of magnitude lower *stellar* central densities than the compact quiescent objects and even some of the star-forming galaxies with significant putative compact cores among the massive $2 < z < 2.6$ NIC2 samples of van Dokkum et al. (2008) and Kriek et al. (2009). This could suggest different paths for the formation of the inner stellar components (see, e.g., Tacconi et al. 2008; Franx et al. 2008, and references therein), with highly dissipative mechanisms (such as major mergers) being more important in the latter samples and secular processes dominating for our SINS NIC2 sample.

The sample presented in this work is small and spans a modest range in galaxy parameters, but our analysis highlights some of the key issues that will be important to address in future studies. The identification of clumps at different wavelengths can potentially probe a wider range in clump properties and evolutionary stage. Larger samples probing a wider range in host galaxy properties and including (major) mergers as well will clearly allow better exploration of trends of clump properties with galaxy parameters, evolutionary stage, and location within the host galaxy, and assessment of possible differences between clumps in disks and in merging systems. The combination of M/L-sensitive and age-sensitive properties will be crucial to make progress. One of the currently most important limitations in the interpretation of the clump properties is their unknown SFH. Tighter constraints on clump masses, star formation and outflow rates, and internal structure and dynamics will provide better insights into the issue of clump lifetimes and their role in the internal dynamical evolution of young galaxies.

We are grateful to our many colleagues for stimulating discussions and insightful comments on various aspects of this work, in particular A. Burkert, P. Johansson, T. Naab, A. Renzini, S. Wuyts, and the entire SINS team. We also wish to thank M. Swinbank and T. Jones for useful discussions and additional information about clumps in their lensed galaxy samples. We thank the referee for a thoughtful report and useful suggestions that improved the presentation of the results. Support for *HST* program no. 10924 was provided by NASA through a grant from the Space Telescope Science Institute, which is operated by the Association of Universities for Research in Astronomy, Inc., under NASA contract NAS 5-26555. N.M.F.S. acknowledges support by the Minerva program of the MPG. A.E.S. acknowledges support from the David and Lucile Packard Foundation. N.B. is supported by the Marie Curie grant PIOF-GA-2009-236012 from the European Commission. G.C. acknowledges support by ASI-INAF grant I/009/10/0. A.S. thanks the DFG for support via German-Israeli Project Cooperation Grant STE1868/1-1.GE625/15.1.

APPENDIX

VARIATIONS OF CLUMP STELLAR AGES WITH DIFFERENT STAR FORMATION HISTORIES FOR BX 482

In Sections 4.2 and 5.2, we used the Hα equivalent width, with the continuum flux density approximated from the H_{160}-band photometry of our targets, to derive stellar ages for the clumps and interclump regions in BX 482. This indicator is nearly insensitive to interstellar dust reddening if differential extinction is negligible, i.e., if the Hα line emission from the H II regions is attenuated by the same amount as the continuum light from the stellar population. On the other hand, the $W^{\rm rest}$(Hα) depends sensitively on the SFH. The analysis throughout the paper relies on the simple assumption of CSF with age. Here, we

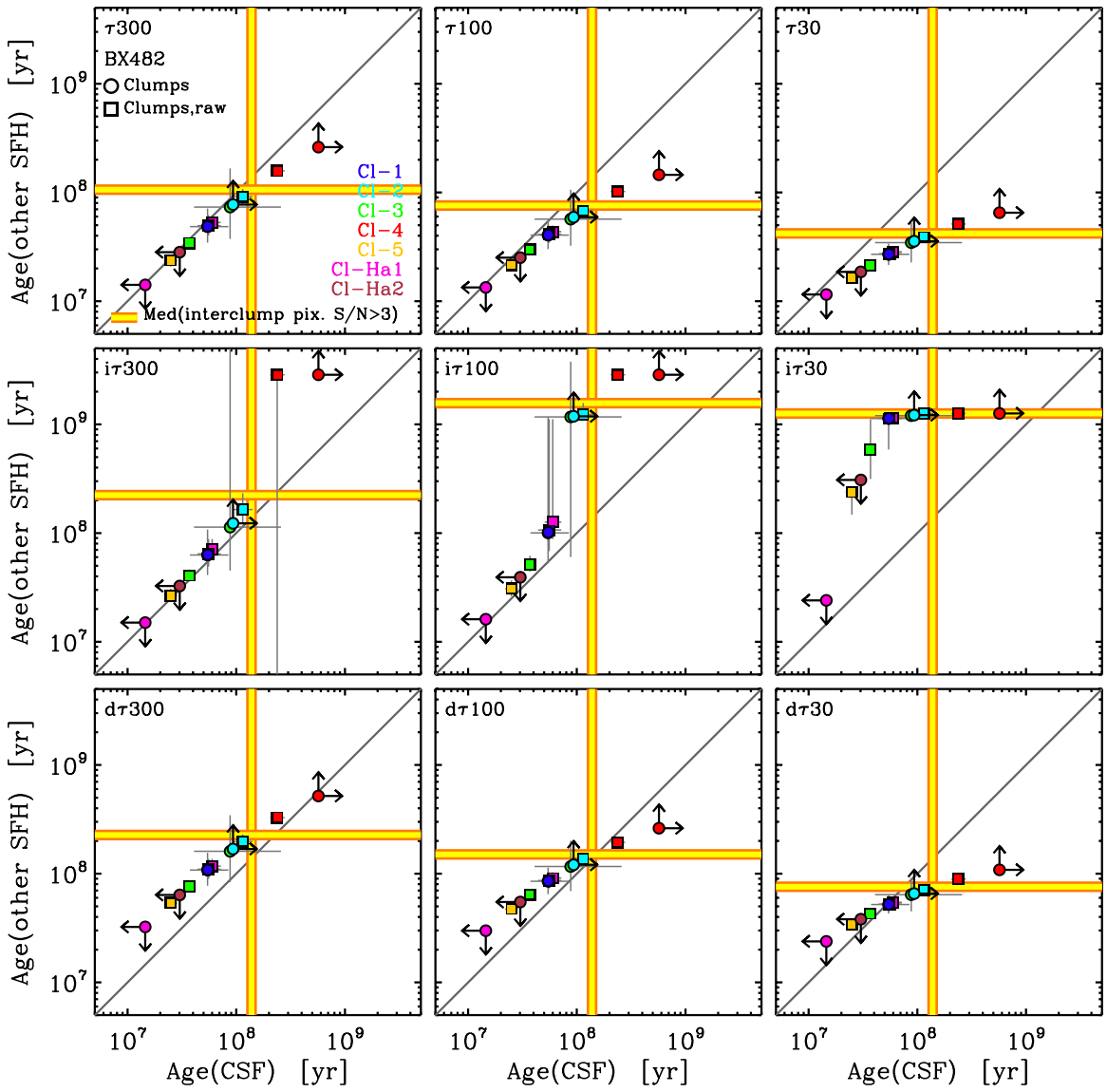

Figure 11. Comparison of stellar ages of clumps in BX 482 derived from their Hα equivalent width for different assumptions on the star formation history (SFH), as described in the Appendix. In all panels, the horizontal axis corresponds to the age derived for a constant star formation (CSF) rate. The vertical axis corresponds to the age derived for alternative SFHs as follows. Top row: exponentially declining star formation rates with e-folding timescales $\tau = 300$, 100, and 30 Myr (labeled "τ300," "τ100," and "τ30," respectively, in each panel). Middle row: exponentially increasing star formation rates with the same e-folding timescales (labeled "iτ300," "iτ100," and "iτ30," respectively). Bottom row: "delayed" star formation rates with the same e-folding timescales (labeled "dτ300," "dτ100," and "dτ30," respectively). Results based on the background-subtracted and raw clump photometry are plotted as circles and squares, respectively. Different colors indicate different clumps, as labeled in the top left panel. Uncertainties of the ages are computed by propagating the measurement uncertainties on the model curves. The thick yellow–orange lines in each panel show the stellar age derived from the median Hα equivalent width of pixels in the interclump regions with an S/N > 3 in H_{160} band and Hα emission.

(A color version of this figure is available in the online journal.)

explore the effects of adopting other SFHs on the interpretation of the $W^{\rm rest}$(Hα).

For this purpose, we used the same Bruzual & Charlot (2003) models of solar metallicity, with the Chabrier (2003) IMF and the Calzetti et al. (2000) reddening law as for the SED modeling of the integrated rest-UV/optical SED of our SINS NIC2 sample galaxies. We investigated three different generic forms for the SFH: (1) exponentially declining models with SFR(t) $\propto$ exp ($-t/\tau$) ("τ" models), (2) exponentially increasing models with SFR(t) $\propto$ exp (t/τ) ("inverted τ," or "iτ" models), and (3) a hybrid case with SFR(t) $\propto$ (t/τ) exp ($-t/\tau$) ("delayed τ," or "dτ" models), where SFR is the star formation rate, t is the time elapsed since the onset of star formation (taken as the age of the stellar population), and τ is the characteristic timescale of the star formation. A CSF corresponds, for the exponentially declining parameterization, to $\tau \rightarrow \infty$. We computed suites of models for a range of τ from 10 Myr to 1 Gyr. For all SFHs, the $W^{\rm rest}$(Hα) decreases monotonically with age; differences are in the shape of the curves.

We derived the stellar ages and uncertainties of the clumps in BX 482 from the $W^{\rm rest}$(Hα) and their 1σ errors (projected onto the model curves). We always assumed a fixed maximum age possible corresponding to the age of the universe at the redshift of BX 482. Ages older than the universe are formally obtained only for NIC2 clump 4, with lowest $W^{\rm rest}$(Hα), and inverted τ models with timescales $\gtrsim$100 Myr. This suggests that either such SFHs are inappropriate or there is significant differential attenuation between the Hα line and stellar continuum

emission; the data currently available do not allow us to distinguish between these two possibilities. Figure 11 illustrates the differences in ages obtained for each SFH family and three representative timescales, $\tau = 30$, 100, and 300 Myr, plotted as a function of the ages for CSF models. Because of the monotonic variations with t irrespective of the SFH, the relative age differences between clumps are qualitatively preserved for any given SFH. The range of ages tends to become narrower for shorter star formation timescales. However, the uncertainties of the measurements are typically sufficiently small that the age variations among the clumps remain significant for all τ values considered. This result holds independently of the treatment of the background light from the host galaxy; the measurements based on the "background-subtracted" photometry lead to larger age differences than those based on the "raw" photometry, i.e., not accounting for the contribution of the underlying host stellar population to the clump light.

From this exploration of the impact of SFHs on the interpretation of the $W^{\rm rest}({\rm H}\alpha)$, we conclude the following. While the absolute ages of the clumps in BX 482 and ranges thereof depend on the SFH, the relative age variations are qualitatively robust and quantitatively significant in view of the measurements uncertainties. This conclusion is valid as long as the SFHs of individual clumps are similar in their general time dependence and in their timescale. Verifying this assumption would be important but obviously, detailed constraints on clump SFHs would require much more extensive multi-wavelength data sets at high angular resolution. Future studies with *HST*/WFC3 and later with *James Webb Space Telescope* and the Extremely Large Telescopes should be able to provide such constraints and further insights in the detailed SFH across individual galaxies, thereby also allowing more accurate reconstruction of the galaxy-wide global SFH, one of the major uncertainty in SED modeling of distant objects.

REFERENCES

Agertz, O., Teyssier, R., & Moore, B. 2009, MNRAS, 397, L64
Aumer, M., Burkert, A., Johansson, P. H., & Genzel, R. 2010, ApJ, 719, 1230
Blanton, M. R., Dalcanton, J., Eisenstein, D., et al. 2001, AJ, 121, 2358
Bonnet, H., Abuter, R., Baker, A., et al. 2004, Messenger, 117, 17
Bouché, N., Cresci, G., Davies, R., et al. 2007, ApJ, 671, 303
Bournaud, F., & Combes, F. 2002, A&A, 392, 83
Bournaud, F., Daddi, E., Elmegreen, B. G., et al. 2008, A&A, 486, 741
Bournaud, F., Elmegreen, B. G., & Elmegreen, D. M. 2007, ApJ, 670, 237
Bruzual, A. G., & Charlot, S. 2003, MNRAS, 344, 1000
Bussmann, R. S., Dey, A., Lotz, J., et al. 2009, ApJ, 693, 750
Calzetti, D., Armus, L., Bohlin, R. C., et al. 2000, ApJ, 533, 682
Cameron, E., Carollo, C. M., Oesch, P. A., et al. 2010, ApJ, submitted (arXiv:1007.2422)
Carollo, C. M., Scarlata, C., Stiavelli, M., Wyse, R. F. G., & Mayer, L. 2007, ApJ, 658, 960
Ceverino, D., Dekel, A., & Bournaud, F. 2010, MNRAS, 404, 2151
Chabrier, G. 2003, PASP, 115, 763
Colley, W. N., Rhoads, J. E., Ostriker, J. P., & Spergel, D. N. 1996, ApJ, 473, L63
Conselice, C. J., Grogin, N. A., Jogee, S., et al. 2004, ApJ, 600, L139
Cowie, L., Hu, E., & Songaila, A. 1995, AJ, 110, 1576
Cresci, G., Hicks, E. K. S., Genzel, R., et al. 2009, ApJ, 697, 115
Daddi, E., Bournaud, F., Walter, F., et al. 2010, ApJ, 713, 686
Dasyra, K. M., Yan, L., Helou, G., et al. 2008, ApJ, 680, 232
Dekel, A., Sari, R., & Ceverino, D. 2009, ApJ, 703, 785
Dib, S., Bell, E., & Burkert, A. 2006, ApJ, 638, 797
Eisenhauer, F., Tecza, M., Thatte, N., et al. 2003, Messenger, 113, 17
Elbaz, D., Hwang, H. S., Magnelli, B., et al. 2010, A&A, 518, L29
Elmegreen, B. G. 2009, in IAU Symp. 254, The Galaxy Disk in Cosmological Context, ed. J. Andersen, J. Bland-Hawthorn, & B. Nordström (Cambridge: Cambridge Univ. Press), 289
Elmegreen, B. G., Bournaud, F., & Elmegreen, D. M. 2008, ApJ, 688, 67
Elmegreen, B. G., & Elmegreen, D. M. 2005, ApJ, 627, 632
Elmegreen, B. G., Elmegreen, D. M., Fernandez, M. X., & Lemonias, J. J. 2009a, ApJ, 692, 12
Elmegreen, B. G., Elmegreen, D. M., & Hirst, A. C. 2004a, ApJ, 612, 191
Elmegreen, D. M., Elmegreen, B. G., Marcus, M. T., et al. 2009b, ApJ, 701, 306
Elmegreen, D. M., Elmegreen, B. G., Ravindranath, S., & Coe, D. A. 2007, ApJ, 658, 763
Elmegreen, D. M., Elmegreen, B. G., Rubin, D. S., & Schaffer, M. A. 2005, ApJ, 631, 85
Elmegreen, D. M., Elmegreen, B. G., & Sheets, C. M. 2004b, ApJ, 603, 74
Épinat, B., Amram, P., Balkowski, C., & Marcelin, M. 2010, MNRAS, 401, 2113
Épinat, B., Contini, T., Le Fèvre, O., et al. 2009, A&A, 504, 789
Erb, D. K., Steidel, C. C., Shapley, A. E., et al. 2006, ApJ, 646, 107
Escala, A., & Larson, R. B. 2008, ApJ, 685, L31
Förster Schreiber, N. M., Genzel, R., Bouché, N., et al. 2009, ApJ, 706, 1364
Förster Schreiber, N. M., Genzel, R., Lehnert, M. D., et al. 2006, ApJ, 645, 1062
Förster Schreiber, N. M., Shapley, A. E., Erb, D. K., et al. 2011, ApJ, 731, 65, (Paper I)
Franx, M., van Dokkum, P. G., Förster Schreiber, N. M., et al. 2008, ApJ, 688, 770
Genzel, R., Burkert, A., Bouché, N., et al. 2008, ApJ, 687, 59
Genzel, R., Newman, S., Jones, T., et al. 2011, ApJ, 733, 101
Genzel, R., Tacconi, L. J., Eisenhauer, F., et al. 2006, Nature, 442, 786
Genel, S., Naab, T., Genzel, R., et al. 2010, ApJ, submitted (arXiv:1011.0433)
Giavalisco, M., Livio, M., Bohlin, R. C., Duccio Macchetto, F., & Stecher, T. P. 1996, AJ, 112, 369
Hummer, D. G., & Storey, P. J. 1987, MNRAS, 224, 801
Immeli, A., Samland, M., Gerhard, O., & Westera, P. 2004a, A&A, 413, 547
Immeli, A., Samland, M., Westera, P., & Gerhard, O. 2004b, ApJ, 611, 20
Jones, T., Swinbank, A. M., Ellis, R. S., Richard, J., & Stark, D. P. 2010, MNRAS, 404, 1247
Kormendy, J., & Kennicutt, R. C., Jr. 2004, ARA&A, 42, 603
Kriek, M., van Dokkum, P. G., Franx, M., et al. 2008, ApJ, 677, 219
Kriek, M., van Dokkum, P. G., Franx, M., Illingworth, G. D., & Magee, D. K. 2009, ApJ, 705, L71
Krumholz, M. R., & Dekel, A. 2010, MNRAS, 406, 112
Law, D. R., Steidel, C. C., Erb, D. K., et al. 2007, ApJ, 656, 1
Law, D. R., Steidel, C. C., Erb, D. K., et al. 2009, ApJ, 697, 2057
Lin, D. N. C., & Pringle, J. E. 1987, ApJ, 320, L87
Lotz, J. M., Primack, J., & Madau, P. 2004, AJ, 128, 163
Mancini, C., Förster Schreiber, N. M., Renzini, A., et al. 2011, ApJ, submitted
Murray, N., Quataert, E., & Thompson, T. A. 2010, ApJ, 709, 191
Muzzin, A., van Dokkum, P. G., Kriek, M., et al. 2010, ApJ, 725, 742
Noguchi, M. 1999, ApJ, 514, 77
Nordon, R., Lutz, D., Shao, L., et al. 2010, A&A, 518, L24
Nordon, R., Lutz, D., Berta, S., et al. 2011, ApJ, submitted (arXiv:1106.1186)
Overzier, R. A., Heckman, T. M., Schiminovich, D., et al. 2010, ApJ, 710, 979
Papovich, C., Dickinson, M., Giavalisco, M., Conselice, C. J., & Ferguson, H. C. 2005, ApJ, 631, 101
Peter, A. H. G., Shapley, A. E., Law, D. R., et al. 2007, ApJ, 668, 23
Reddy, N. A., Erb, D. K., Pettini, M., Steidel, C. C., & Shapley, A. E. 2010, ApJ, 712, 1070
Shapiro, K. L., Genzel, R., Förster Schreiber, N. M., et al. 2008, ApJ, 682, 231
Shapley, A. E., Erb, D. K., Pettini, M., Steidel, C. C., & Adelberger, K. L. 2004, ApJ, 612, 108
Silk, J. 2001, MNRAS, 324, 313
Stark, D. P., Swinbank, A. M., Ellis, R. S., et al. 2008, Nature, 455, 775
Steidel, C. C., Shapley, A. E., Pettini, M., et al. 2004, ApJ, 604, 534
Stetson, P. B. 1987, PASP, 99, 191
Swinbank, A. M., Smail, I., Chapman, S. C., et al. 2010a, MNRAS, 405, 234
Swinbank, A. M., Smail, I., Longmore, S., et al. 2010b, Nature, 464, 733
Tacconi, L. J., Genzel, R., Neri, R., et al. 2010, Nature, 463, 781
Tacconi, L. J., Genzel, R., Smail, I., et al. 2008, ApJ, 680, 246
Toft, S., van Dokkum, P., Franx, M., et al. 2007, ApJ, 671, 285
van den Bergh, S., Abraham, R. G., Ellis, R. S., et al. 1996, AJ, 112, 359
van Dokkum, P. G., Franx, M., Kriek, M., et al. 2008, ApJ, 677, L5
Wright, S. A., Larkin, J. E., Barczys, M., et al. 2007, ApJ, 658, 78
Wright, S. A., Larkin, J. E., Law, D. R., et al. 2009, ApJ, 699, 421
Wuyts, S., Förster Schreiber, N. M., Lutz, D., et al. 2011, ApJ, in press (arXiv:1106.5502)
Yoshikawa, T., Akiyama, M., Kajisawa, M., et al. 2011, ApJ, 718, 112